Age-related microstructural and physiological changes in normal brain measured by MRI γ-metrics derived from anomalous diffusion signal representation

Michele Guerreri [a,b,*], Marco Palombo [b,c], Alessandra Caporale [b,d], Fabrizio Fasano [e], Emiliano Macaluso [f], Marco Bozzali [g], Silvia Capuani [b,g]

[a] SAIMLAL Department, Sapienza, Piazzale Aldo Moro, 5, 00185, Roma, RM, Italy
[b] Institute for Complex Systems, CNR, Rome, Italy
[c] Department of Computer Science & Centre for Medical Image Computing, University College London, London, United Kingdom
[d] Laboratory for Structural, Physiologic and Functional Imaging, Perelman School of Medicine University of Pennsylvania, Philadelphia, PA, USA
[e] Department of Neuroscience, Parma University, Parma, Italy
[f] ImpAct Team, Lyon Neuroscience Research Center, Lyon, France
[g] Neuroimaging Laboratory, Santa Lucia Foundation, Rome, Italy

ARTICLE INFO

ABSTRACT

Nowadays, increasing longevity associated with declining cerebral nervous system functions, suggests the need for continued development of new imaging contrast mechanisms to support the differential diagnosis of age-related decline.

In our previous papers, we developed a new imaging contrast metrics derived from anomalous diffusion signal representation and obtained from diffusion-weighted (DW) data collected by varying diffusion gradient strengths. Recently, we highlighted that the new metrics, named γ-metrics, depended on the local inhomogeneity due to differences in magnetic susceptibility between tissues and diffusion compartments in young healthy subjects, thus providing information about myelin orientation and iron content within cerebral regions. The major structural modifications occurring in brain aging are myelinated fibers damage in nerve fibers and iron accumulation in gray matter nuclei. Therefore, we investigated the potential of γ-metrics in relation to other conventional diffusion metrics such as DTI, DKI and NODDI in detecting age-related structural changes in white matter (WM) and subcortical gray matter (scGM). DW-images were acquired in 32 healthy subjects, adults and elderly (age range 20–77 years) using 3.0T and 12 b-values up to 5000 s/mm^2. Association between diffusion metrics and subjects' age was assessed using linear regression. A decline in mean γ (Mγ) in the scGM and a complementary increase in radial γ (γ⊥) in frontal WM, genu of corpus callosum and anterior corona radiata with advancing age were found. We suggested that the increase in γ⊥ might reflect declined myelin density, and Mγ decrease might mirror iron accumulation. An increase in $D_{//}$ and a decrease in the orientation dispersion index (ODI) were associated with axonal loss in the pyramidal tracts, while their inverted trends within the thalamus were thought to be linked to reduced architectural complexity of nerve fibers. γ-metrics together with conventional diffusion-metrics can more comprehensively characterize the complex mechanisms underlining age-related changes than conventional diffusion techniques alone.

1. Introduction

The human brain undergoes regional-specific structural and physiological changes during lifespan, which are reflected in a decline in cognitive abilities that become less and less efficient with aging (Lockhart et al., 2014). Axonal damage and disintegration, loss of neuronal cells, myelin degradation and iron accumulation (Draganski et al., 2011; Xu et al., 2008; Ashraf et al., 2018) are the main age-related modifications that inexorably occur in the aging brain. With increasing life expectancy in developed countries, there is a great need to establish efficient

---

protocols for the early diagnosis of cerebral decline that can support the development of new drugs and new therapies for both normal and pathological aging.

In the last decades, magnetic resonance diffusion imaging (MRI) techniques and in particular diffusion tensor imaging (DTI) studies (Basser et al., 1994) have contributed to the neuroscience of normal ageing and to characterizing changes in morphology and tissues that occur with advancing age. From the fourth decade of life, DTI metrics highlighted a decline in fractional anisotropy (FA) and a complementary increase in mean diffusivity (MD) in cerebral white matter (WM) due to aging (Salat et al., 2005). This behavior of the DTI parameters reflects loss of WM fibers and of their directionality and a reduction in axonal diameters (Bartzokis et al., 2012; Callaghan et al., 2014). On the other hand, DTI investigations into cerebral gray matter (GM) as a function of subjects' age, showed less clear patterns (Rathi et al., 2014; Salminen et al., 2016), whereas T1, T2 and T2* weighted imaging and susceptibility-based imaging studies highlighted GM atrophy together with an increase in iron content in specific GM regions (Pfefferbaum et al., 2010; Haacke et al., 2010; Daugherty and Raz, 2015; Pirpamer et al., 2016). DTI parameters quantify the diffusive properties of bulk water poorly interacting with the complex structure of the neural tissue, so DTI metrics have a limited sensitivity and specificity in the detection of early microstructural changes in WM and GM. Moreover, the evaluation of early physiological modification due to different iron content in vivo is challenging and still requires further investigation (Pfefferbaum et al., 2010). As a consequence, in the last few years, several methods have been developed to increase the potential ability of MRI diffusion techniques in detecting rearrangement of WM and its modification due to normal and pathological aging, each with its strengths and weaknesses (Jelescu and Budde, 2017). Two complementary approaches have emerged for extracting information on the tissue microstructure exploiting the biological water diffusion signal: signal representation and biophysical tissue modeling (Jelescu and Budde, 2017; Novikov et al., 2018). On the one hand, signal representation or "statistical models" such as DTI and diffusion kurtosis imaging (DKI) quantify parameters deriving from statistical mechanics without assumptions about the underlying tissue, but they lack specificity, and provide only an indirect characterization of the microstructure (Kiselev, 2017). On the other hand, biophysical tissue models such as neurite orientation distribution and density imaging (NODDI) require schematic-geometric assumptions about the underlying tissues. Therefore, even if such models can potentially provide greater specificity and interpretation of biologically relevant parameters, the results are dramatically dependent on the initial geometric assumptions that in general may not well describe the main components of tissue microstructures, especially their changes due to pathologies (Novikov et al., 2018). Since DKI is sensitive to water molecules which interact more with the cerebral microstructures than those of bulk water considered in DTI, Kurtosis techniques have been used to study healthy aging as an extension of DTI as these techniques are more sensitive to microstructural changes (Coutu et al., 2014; Gong et al., 2014; Lätt et al., 2013).

In parallel, several strategies have been developed to quantify the differences in magnetic susceptibility ($\Delta\chi$) in brain tissues that potentially offer the possibility to measure the presence of heavy metals, such as iron in GM and WM, and to highlight the directionality, the microarchitecture and the chemical arrangement of the neural tissues. As an example, quantitative susceptibility mapping (QSM) allows the calculation of bulk magnetic susceptibility distribution of tissues in vivo from gradient echo (GRE) magnetic resonance phase images (Langkammer et al., 2012) while susceptibility tensor imaging (STI) quantifies the amount of $\Delta\chi$ anisotropy (Liu, 2010). However, in order to compute the susceptibility tensor, it is necessary to acquire the signal along at least six different orientations of the sample with respect to the static magnetic field (B_0) (Liu, 2010). This is an intrinsic limitation of STI imaging, since subject rotation during acquisition is hardly practicable in clinical applications.

Recently, we showed the potential of the new γ-metrics derived from anomalous diffusion (AD) signal representation in highlighting $\Delta\chi$ in myelin orientation and iron contents within selected regions of WM and subcortical GM (scGM), respectively (Caporale et al., 2017). Because the pseudo-superdiffusion γ parameter depends on the local $\Delta\chi$ at the interface between different tissues and on the distribution and dimension of the diffusion compartments, the γ-metrics could be useful for extracting information complementary to that of the DTI in normal aging studies of the human brain.

Starting from the representation of the diffusion weighted (DW) signal in terms of fractional derivatives (Lin, 2015, 2016, 2018), we quantified the γ parameters using the signal, S(b), obtained with a pulse field gradient (PFG) sequence collected by changing diffusion gradient (g_{diff}) strength at a constant value of the diffusion time Δ. In this framework, DW signal must be fitted to the stretched exponential function: $S(b) = S(0)exp(-(bD)^{\gamma})$ (Magin et al., 2008; De Santis et al., 2011; Hall and Barrick, 2012; Ingo et al., 2014). In the context of the transient anomalous diffusion theory, based on the Continuous time random walk (CTRW) (Metzler and Klafter, 2000), the γ parameter extracted by fitting the above function to DW data, quantifies superdiffusion processes. Clearly, there is no superdiffusion of water in brain tissues, but the signal representation that we use to quantify γ reflects the additional effect of the magnetization phasing and dephasing due to internal gradients (g_{int}) generated by $\Delta\chi$ at the interface between different tissues. As explained in our previous papers describing *in vitro* and *ex vivo* experiments to validate the γ-metrics (Palombo et al. 2011, 2012; Capuani et al., 2013), an ensemble of spins in a voxel can contribute to a further decrease in the DW signal attenuation, when g_{int} and g_{diff} are in the same order of magnitude; other spins (that can be located in a voxel far from the first ones) can acquire a phase that will help to increase the signal. Due to indistinguishable spins associated with water molecules, this scenario mimics a super-diffusion regime where water molecules seem to perform longer jumps because their signal disappear in one spot, while appearing instantaneously in another spot. For this reason, we named γ the pseudo-superdiffusion parameter of transient anomalous diffusion. The adjective "transient" means that over a sufficiently long time, diffusion asymptotically becomes normal (or Gaussian) showing a finite asymptotic diffusion value (percolation limit). In this paper, the potential of γ-metrics in detecting WM and scGM changes due to aging is shown regardless of the debate concerning the existence of transient anomalous diffusion in brain tissues (Nicholson, 2015; Saxton, 2008; Destainville et al., 2008), as this issue is outside the scope of this study. Towards this goal, γ-metric results in WM and scGM were compared to DTI parameters, mean kurtosis (MK) derived from DKI metrics (Jensen et al., 2005) and NODDI derived parameters (Zhang et al., 2012). Association between diffusion metrics and subjects' age was assessed *via* linear regression. We tested the hypothesis whereby γ-metrics are sensitive to physiological and structural variations that occur in the human brain during aging, such as iron deposition and myelin degradation.

2. Materials and methods

2.1. Studied population

A total of 35 volunteers took part in this study after providing informed written consent in compliance with the national laws and with the local ethics committee guidelines. None in the cohort had a history of stroke, head injuries, medical illness or diagnosis of neurological and psychiatric disorders. Of the 35 volunteers, 32 were retained for this study, 19 men and 13 women (age range 20–77 years, Mean $\pm$ SD = 43.7 $\pm$ 18.2y). One of the volunteers was excluded due to the presence of brain abnormalities. The other two subjects were discarded because of incomplete data acquisitions and substantial bulk motion.

2.2. Data acquisition

All volunteers underwent MRI examination using a 3.0T Siemens Magnetom Allegra (Siemens Medical Solutions, Erlangen, Germany) equipped with a circularly polarized transmit-receive coil. The maximum gradient strength was 40 mT/m with a maximum slew rate of 400 T/m/s. The same MRI protocol was applied to all subjects, including whole-brain T1-weighted images and Diffusion-Weighted Spin Echo-Echo Planar Imaging (DW SE-EPI). Care was taken to center each subject's head in the head coil and to restrain subject's motion with cushions and medical tape.

Diffusion experiments were performed with the following parameters: $TR/TE = 6400/107$ ms; $\Delta/\delta = 107/35$ ms; bandwidth $= 1860$ Hz/px; matrix size $= 128 \times 128$, number of axial slices $= 32$; in-plane resolution $= 1.8 \times 1.8$ mm^2; slice thickness $= 3$ mm; number of averaged scans NS $= 2$. The diffusion-encoding gradients were applied along 15 non-collinear directions spanning the entire sphere to minimize the effect of cross-terms between the diffusion gradients and the imaging gradients in the estimation of diffusion parameters (Kingsley, 2006). The set of 15 diffusion directions was chosen among the optimized schemes suggested by Landman et al. being one of the possible minimum potential energy partitions of the scheme of 30 directions proposed by Jones et al., based on the electrostatic repulsion algorithm (Landman et al., 2007; Jones et al., 1999). By varying the gradient strength **g**, 11 different b-values were acquired (b $= 200, 400, 600, 800, 1000, 1500, 2000, 2500, 3000, 4000, 5000$ s/mm^2), plus the b0 image with no diffusion weighting, with an anterior-posterior phase encoding direction for all the scans. The

acquisition time for the entire diffusion protocol was approximately 37 min per subject.

2.3. Data analysis

Fig. 1 illustrates the main steps of the image processing pipeline used in this study. After the raw data quality check, all diffusion images were pre-processed to correct for noise effects, Gibbs ringing artifacts, eddy currents and subject's movements. DTI, DKI, NODDI and γ-imaging representative functions (see paragraph 2.4) were fitted to different subsets of the diffusion data. A population-based template was constructed, and all images were co-registered to this template. The analysis was finally carried out using both a ROI-based and a voxel-wise based approach.

2.3.1. Pre-processing

All diffusion images were first visually inspected to check for data quality. Datasets with considerable bulk motion artifacts were discarded.

To reduce the noise effect on the diffusion parameter estimation, the MRtrix3 *dwidenoise* tool (Copyright ©2016 New York University, University of Antwerp, https://github.com/MRtrix3/mrtrix3) was applied as the first step of the preprocessing (Tournier et al., 2012; Veraart et al., 2016a, 2016b). Then, the Gibbs ringing correction framework of Kellner et al. (2016) was applied for EPI distortion correction. Finally, the image distortions induced by head motion and eddy currents were corrected using the FSL eddy tool (FMRIB Software Library v5.0, FMRIB, Oxford,
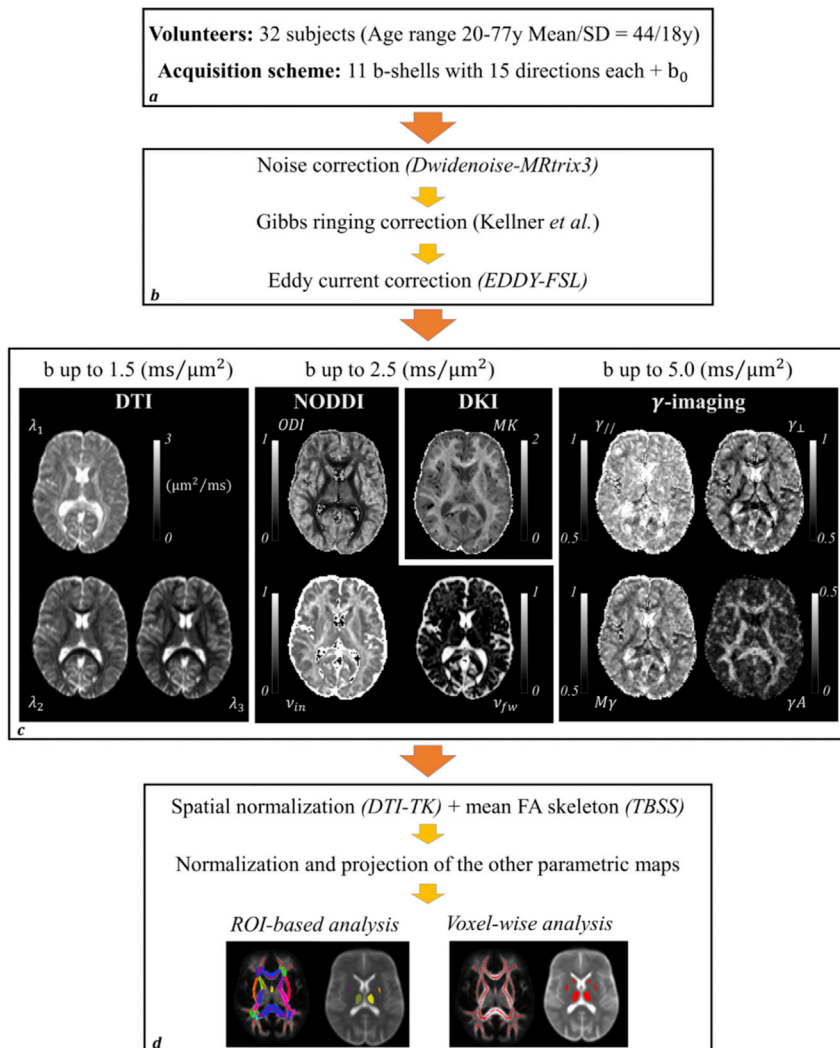
Fig. 1. Pipeline of the data processing: the main steps carried out to analyze the diffusion weighted images are schematically summarized. *a*) Brief description of the subjects' cohort and acquisition protocol. *b*) The collected data were then corrected for random noise effects, Gibbs ringing artifacts, movements and eddy current induced artifacts. *c*) Different subsets of the data were used to obtain the different diffusion metrics. *d*) The DT-eigenvalues were used to obtain a population specific template; all the other metrics were then projected onto this template. Associations between subjects' age and diffusion metrics were assessed averaging over regions of interest (ROIs) or voxel-wise.

UK) (Yamada et al., 2014; Andresson and Sotiropoulos, 2016).

2.4. Diffusion metrics generation

Different subsets of the pre-processed data were used to compute DTI, DKI, NOODI and γ-imaging diffusion metrics.

2.4.1. DTI and DKI

The cumulant expansion of the log-transformed diffusion weighted signal in powers of b is the most widespread signal representation. By truncating the expansion at the second order in b, the following expression in tensorial form can be obtained (Basser et al., 1994; Jensen et al., 2005):

$$\ln \frac{\boldsymbol{S}(\boldsymbol{b},\boldsymbol{g})}{\boldsymbol{S}_0} = -\boldsymbol{b}\sum_{i,j=1}^{3}\boldsymbol{g}_i\boldsymbol{g}_j\boldsymbol{D}_{ij} + \frac{1}{6}\boldsymbol{b}^2\left(\sum_{i=1}^{3}\frac{\boldsymbol{D}_{ii}}{3}\right)\sum_{i,j,k,l=1}^{3}\boldsymbol{g}_i\boldsymbol{g}_j\boldsymbol{g}_l\boldsymbol{g}_k\boldsymbol{W}_{ijkl} \tag{1}$$

Here $\boldsymbol{g}$ is the direction of the applied diffusion weighting, $\boldsymbol{D}$ is the rank-2 diffusion tensor and $\boldsymbol{W}$ is the rank-3 kurtosis tensor. For moderate b-values, the above expression can be truncated at the first order, recovering the conventional diffusion tensor imaging (DTI) (Basser et al., 1994).

In this study, DTI analysis was performed *via* FSL dtifit tool, considering the b-shells between $b = 200$ and $b = 1500$ s/mm^2 (i.e. 6 b-values). The dtifit routine returns MD and FA maps together with the three diffusion tensor eigenvalues (λ_1, λ_2, λ_3, with $\lambda_1 > \lambda_2 > \lambda_3$) and eigenvectors ($V_1$, V_2, V_3), which define the DTI reference frame (DTI-rf) voxel-wise. The axial (D//) and radial (D⊥), diffusivities were computed as follows: $D// = \lambda_1$, $D⊥ = (\lambda_2 + \lambda_3)/2$.

By fitting equation (1) to the logarithm of the signal, having acquired at least 21 measures distributed over two b-shells, it is possible to reconstruct the kurtosis tensor $\boldsymbol{W}$ (Jensen et al., 2005). Diffusion kurtosis imaging (DKI) is a clinically feasible extension of DTI at higher b-values that probes restricted water diffusion in tissues providing information about the tissue complexity.

In this work, we used the b-shells up to the $b = 2500$ s/mm^2 to get mean kurtosis (MK) weighted maps. In order to obtain these maps we used the dki_lls method from the *md-dmri* software (https://github.com/markus-nilsson/md-dmri/tree/master/methods). After obtaining the $\boldsymbol{W}$ tensor components, MK was calculated voxel-wise as the average of $\boldsymbol{W}$ elements across the sphere, in a fast and robust way (Hansen et al., 2013).

2.4.2. NODDI

The NODDI model function (Zhang et al., 2012) was fitted to all the b-shells up to $b = 2500$ s/mm^2, using the toolbox available online (https://www.nitrc.org/projects/noddi_toolbox). NODDI is a biophysical tissue model for DW data that aims to infer specific information about the tissue micro-structure. The normalized total diffusion signal, A, is expressed as the sum of contributions from different comportments:

$$A = (1 - \nu_{fw})[(1 - \nu_{in})A_{en} + \nu_{in}A_{in}] + \nu_{fw}A_{fw}, \tag{2}$$

where A_{in} and ν_{in} represent the intra-neurite normalized signal and volume fraction, A_{en} is the extra-neurite normalized signal and A_{fw} and ν_{fw} represent the normalized signal and volume fraction of the compartment modeling isotropic free-water contributions to the signal (such as cerebrospinal fluid). Fitting NODDI to DW-data makes it possible to obtain an estimate of ν_{in} and ν_{fw}, with values comprised between 0 and 1. Moreover, NODDI quantifies the so-called orientation dispersion index (ODI) that attempts to estimate the orientation dispersion of the neurites within each voxel. ODI values run from 0, referring to an isotropically oriented distribution, to 1, referring to a perfectly coherent bundle of fibers.

2.4.3. γ-imaging

Several theoretical models have been proposed to describe anomalous diffusion phenomena, such as the (CTRW) model (Metzler and Klafter, 2000), the fractional motion (FM) model and others (Metzler et al., 2014). The adaptation of these models to MRI diffusion experiments, permits fitting of experimental DW data to functions containing stretched exponentials and other derived parameters (Magin et al., 2008; Zhou et al., 2010; Ingo et al., 2014; Caporale et al., 2017; Yu et al., 2018; Karaman and Zhou, 2018). Unfortunately, different authors have assigned different nomenclatures to indicate the same parameter, fueling the confusion that characterizes the literature of anomalous diffusion methods in MRI.

Recently, two anomalous diffusion parameters were introduced in NMR: α and γ. α quantifies sub-diffusive processes and it is measured by varying diffusion time Δ in a pulse field gradient (PFG) MRI sequence. Conversely, γ quantifies super-diffusive processes characterized by a divergence of the jump length variance, and it is measured by varying gradient strengths g in a PFG sequence at a fixed value of Δ (Palombo et al., 2011; Capuani et al., 2013). In the present work, we performed diffusion experiments by varying g at a fixed value of Δ. Therefore, super-diffusive processes were quantified. Clearly, no real super-diffusive processes of water in biological tissues exist, but "pseudo-superdiffusion" processes mainly due to a local background gradient derived from $\Delta\chi$ at the interface between different diffusion compartments and to the different diffusion lengths with which the water molecules diffuse in several compartments.

As the diffusion weighted NMR signal is proportional to the Fourier transform (FT) of the motion propagator (MP), for investigating pseudo-superdiffusive processes it is possible to use the following function (Metzler and Klafter, 2000) as FT of the anomalous diffusion MP:

$$W(q,t) \simeq \exp[-K_{2\gamma}|2\pi q|^{2\gamma}\Delta] \tag{3}$$

where $K_{2\gamma}$ is a generalized diffusion constant, whose units are $(ms^{-1})^{2\gamma}$, $q = 1/(2\pi)\Gamma g\delta$ is the wave vector, and $0 < \gamma < 1$. For a fixed value of Δ, the stretched exponential form of signal attenuation as a function of b value can easily be derived from (3). Indeed, by replacing $|2\Delta q|^{2\gamma} = b^{\gamma}/\Delta^{\gamma}$ in (3), the following relations can be obtained:

$$\frac{S(b)}{S(0)} \simeq \exp\left[\frac{K_{2\gamma}}{\Delta^{(\gamma-1)}}b^{\gamma}\right] = \exp\left[\frac{D\,\rho^{2(\gamma-1)}}{\Delta^{(\gamma-1)}}b^{\gamma}\right] = \exp\left[-(D_{eff}b)^{\gamma}\right] \tag{4}$$

where D is the diffusion coefficient, $\rho^{2(\gamma-1)}$ and $\Delta^{(\gamma-1)}$ are fractional order space and time constants that preserve units, and D_{eff} is a generalized effective diffusion constant.

In this study, all the b-shells were used for γ-imaging analysis. To obtain the γ metrics, a custom-made Matlab script (MATLAB R2016b) was used. Specifically, the approach described by Caporale et al. (2017), was used in which the reference frame of the tensor representing the transient anomalous diffusion was assumed to coincide with that of the DTI (DTI-rf) (De Santis et al., 2011; Caporale et al., 2017). The choice of projecting the stretched γ-exponents along the axes of DTI-rf assumes that, to a first approximation, anomalous and normal (i.e. Gaussian) diffusion share the same rotationally invariant reference frame (De Santis et al., 2011). The resulting signal representation showing transient anomalous pseudo-superdiffusion is written as:

$$\frac{S(b)_j}{S(0)} = e^{-\sum_{i=1}^{3}A_i\left(b\left(V_i\cdot g_j\right)\right)^{\gamma_i}} \tag{5}$$

Here j denotes the diffusion direction defined by the gradient vector g_j; i indicates each of the 3 main axes with respect to a diffusive motion along a generic direction which may be decomposed; γ_i and A_i are, respectively, the anomalous diffusion exponents and the generalized diffusion coefficients estimated along the direction identified by the eigenvector V_i in the DTI-rf.

The estimated γ-exponents γ_1, γ_2, γ_3 (with $\gamma_1 > \gamma_2 > \gamma_3$) are adimensional parameters that take values from 0 to 1. γ_i equal to 1 indicates a normal Gaussian diffusion, while values of $\gamma_i < 1$ indicate a departure

from Gaussian diffusion. The following γ-metrics were finally computed: axial-γ ($\gamma_{//} = \gamma_1$), radial-γ ($\gamma_\perp = \frac{\gamma_2 + \gamma_3}{2}$), mean-γ ($M\gamma = \frac{\gamma_1 + \gamma_2 + \gamma_3}{3}$), γ-anisotropy ($\gamma A = \sqrt{\frac{3[(\gamma_1 - M_r)^2 + (\gamma_2 - M_r)^2 + (\gamma_3 - M_r)^2]}{2(\gamma_1^2 + \gamma_2^2 + \gamma_3^2)}}$). Specifically, γ//represents the projection of the anomalous exponent in the direction described by the first eigenvector V_1 of the Gaussian diffusion tensor, whereas $\gamma_\perp$ is derived by an average of the other two orthogonal projections (De Santis et al., 2011).

2.5. Post-processing

2.5.1. Image registration

A registration pipeline similar to that proposed by *Timmers* et al. (Timmers et al., 2016) was used. Briefly, a population-specific template was obtained with DTI-TK software (available on http://www.nitrc.org/projects/dtitk). The algorithm applies a deformable registration to the DTI-derived eigenvalues and improves the registration outcome
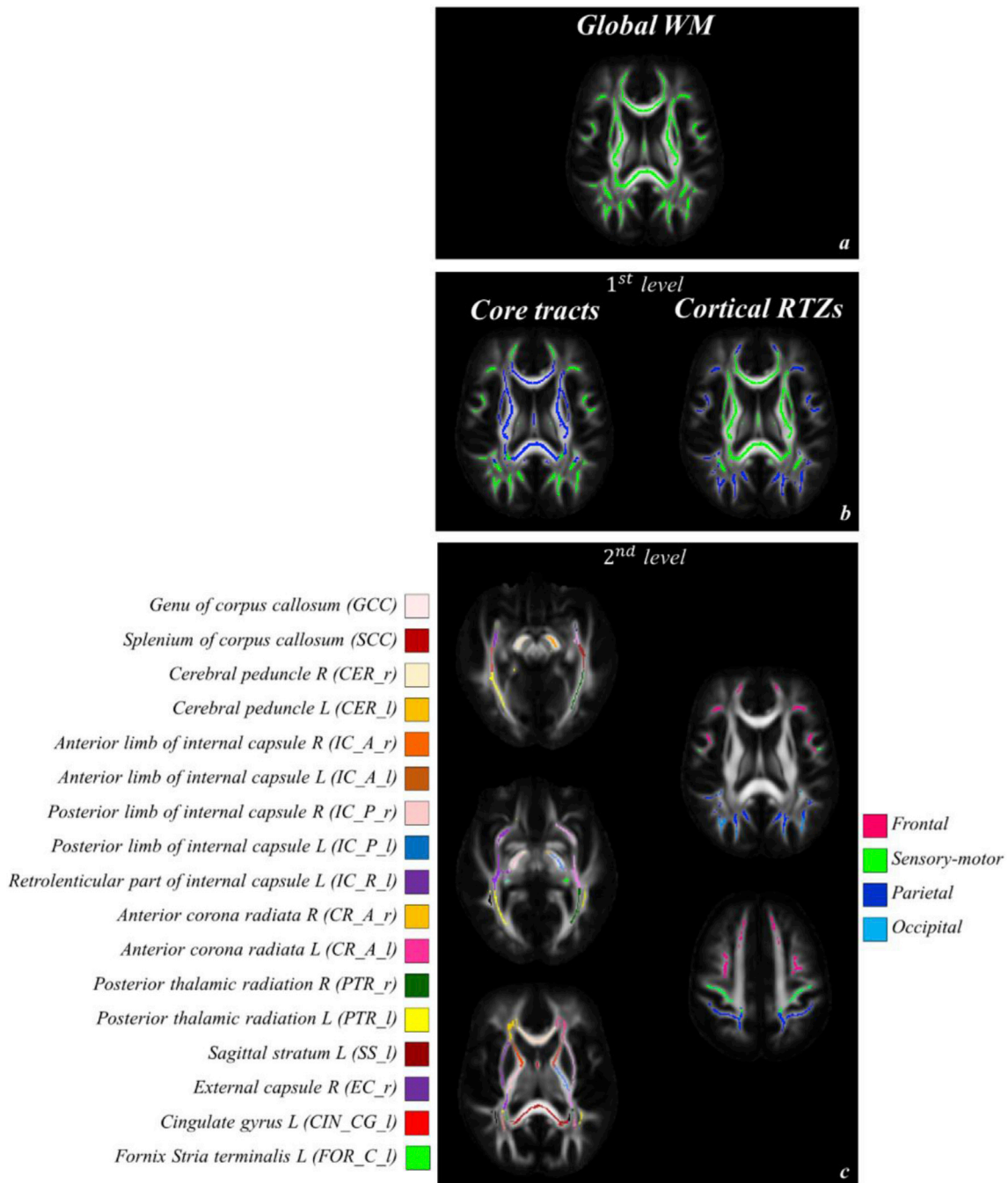
Fig. 2. WM atlas description to illustrate the multi-level ROI-based approach used to analyze and display the results. *a*) the global WM atlas is defined by the skeleton obtained with the skeletonize command of FSL using a threshold of 0.4. *b*) In the first level of the subdivision the core tracts are obtained from the intersection between the WM skeleton, the JHU atlas, while the cortical regional termination zones (RTZs) are obtained from the intersection between the WM skeleton and the Harvard-Oxford cortical atlas. *c*) In the second level of the subdivision, the core tracts and cortical RTZs are further divided into sub-regions according to the atlas nomenclatures; 29 sub-regions for the core tracts and 4 for the cortical RTZs were identified. Only those regions are reported that share at least one association between diffusion metrics and aging.

compared to analogous algorithms based on FA maps (Zhang et al., 2006; Keihaninejad et al., 2013; Wang et al., 2011). The resulting normalized images were used to compute the standard *FA, MD, $D_{//}$* and $D_{\perp}$ maps with a higher resolution compared to the original maps (voxel size $= 1 \times 1 \times 1$ mm^3).

The TBSS tool of FSL (Smith et al., 2006) was used to obtain a mean FA skeleton for the WM tracts common to all subjects in the normalized space. The threshold limit value of this skeleton was set to 0.4 in order to reduce the bias due to cross subject variability of the WM tracts. Finally, the participant-specific transformation fields, obtained during the tensor-based transformation, were used to normalize all the other diffusion metrics used in this study as specified by Timmers et al. in supplementary methods (Timmers et al., 2016).

2.5.2. ROI based analysis

Analysis of the correlation between diffusion metrics and subjects' age was performed on a region of interest (ROI) basis using a hierarchical approach in order to better understand the spatial patterns of aging (Simmonds et al., 2014; Chang et al., 2015). The age-related modifications were calculated separately for WM ROIs and sub-cortical GM (scGM) ROIs.

As regards WM, the global trajectories were first obtained averaging the different metrics along all the voxels belonging to the WM skeleton. Subsequently, two groups of WM regions were selected. Following the nomenclature proposed by Simmonds et al., the "core tracts" were selected as the intersection of the WM skeleton and the JHU-DTI81 atlas (Mori et al., 2008). The "cortical regional termination zones" (RTZs) were defined as the intersection of the cortical GM regions derived from the Harvard-Oxford (HO) atlas in FSL and the WM skeleton. The two groups of WM tracts were further partitioned in sub-tracts. The core tracts were divided using the JHU's own parcellation (http://www.loni.usc.edu/ICBM/Downloads/Downloads_DTI-81.shtml). The cortical RTZs were divided into frontal, sensory-motor, parietal and occipital tracts. All the above steps are summarized in Fig. 2.

Regarding the scGM ROI analysis, the HO subcortical atlas was used to identify the different structures. To avoid partial volume effects each element from the atlas was eroded *via* the "-ero" routine of fslmaths in FSL, using a spherical filter with a 2 mm radius. Because of the limited field of view in the axial direction, only the inner structures of the subcortical GM were retained for the analysis. The caudate, the thalamus, the putamen and the pallidum were considered in the study. In addition, a global trajectory was obtained from the average of all voxels belonging to the examined regions.

The average of each diffusion metrics was then calculated for each ROI. The association between the resulting values and the subjects' age was assessed *via* linear regression using the free software R (R Core Team 2014 http://www.R-project.org/). Also, the shared variance between any two metrics was assessed for the global trajectories. Correlation was considered statistically significant when the derived p-value was ≤ 0.05 after correcting for family-wise error ($p_{fwe} \leq 0.05$), *i.e.* multiplying p by the number of regions considered in the group under analysis. p-value ≤ 0.05 without controlling for family-wise error ($p \leq 0.05$) were also reported for comparison with relevant regions highlighted in previous studies (Billet et al., 2015; Kodiweera et al., 2016).

2.5.3. Voxel-wise analysis

To test the effect of aging on the diffusion metrics voxel-wise, permutation-based statistics was carried out on both the WM and scGM. All diffusion metric maps were performed with the WM skeleton and the scGM eroded mask, respectively. FSL's randomize command was used with 5000 permutations to generate the statistic maps. The Threshold-Free Cluster Enhancement (TFCE) option was used to correct p-values for family wise errors ($p_{fwe} \leq 0.05$).

	$D_{//}$	$D_{\perp}$	MD	FA	ODI	ν_{fw}	ν_{in}	MK	$\gamma_{//}$	$\gamma_{\perp}$	Mγ	γA
Global WM					0.36			0.37				
Cortical RTZ					0.36			0.43				
Frontal		0.36		0.51	0.44			0.52		0.46	0.45	
Sensory-Motor								0.37	0.51		0.36	
Core Tracts												
CER (l)	0.70		0.50		0.72							0.57
CER (r)	0.59				0.71							0.46
IC_P (r)	0.50				0.48							
IC_P (l)	0.50				0.46							
GCC		0.39		0.42		0.40	0.48	0.37	0.55	0.53		0.54
EC (r)						0.54						0.37
CR_A (r)		0.44		0.43				0.49				
CR_A (l)						0.36	0.35	0.42	0.54	0.45		0.56
PTR (l)								0.47	0.46	0.43	0.42	
CIN_CG (l)								0.44				
PTR (r)	0.42	0.37	0.45			0.41		0.51				
CIN_CG (r)						0.36		0.50				
IC_R (l)	0.44				0.40							
FOR_C (l)	0.41				0.39	0.39	0.43		0.46		0.43	
SS (r)						0.41	0.45				0.36	
SCC								0.40				0.37
IC_A (r)												0.37
SS (l)											0.36	

	$D_{//}$	$D_{\perp}$	MD	FA	ODI	ν_{fw}	ν_{in}	MK	$\gamma_{//}$	$\gamma_{\perp}$	Mγ	γA
Global scGM	0.36			0.53	0.55	0.61	0.48		0.45	0.52	0.53	
Putamen	0.39	0.60	0.55	0.64		0.80	0.72	0.64	0.74	0.79	0.79	0.72
Thalamus	0.56			0.41	0.56	0.39						
Caudate	0.36	0.43	0.44	0.35		0.66	0.67					0.40
Pallidus						0.40						

-1 — Negative — 0 — Positive — 1

Fig. 3. ROI-based results obtained using the multi-level ROI-based analysis in white matter (WM), at the top, and subcortical gray matter (scGM), at the bottom. The colored cells indicate the regions where a correlation between a diffusion parameter and age was found (p 0.05). Warm colors indicate positive correlation, while cold colors indicate negative correlation. Regions showing a significant correlation after correction for family-wise errors are highlighted in bold and by boxes with dashed contours.

3. Results

3.1. ROI analysis

To display the results, we used a figure format like the one used by (Billiet et al., 2015). For each ROI and each diffusion metrics we reported the correlation coefficient when *p* 0.05. Red-yellow colors stood for positive correlation, while blue-cyan colors stood for negative correlation. The regions, where a linear correlation with a family-wise error corrected p-value was found significant ($p_{fwe} < 0.05$), were highlighted in bold and by boxes with dashed contours. Fig. 3 shows the results for WM ROIs (at the top) and scGM (at the bottom), whereas Fig. 4 shows plots of different diffusion metrics *vs* subjects' age in different regions of WM and scGM.

3.1.1. Results in WM

$D_{//}$ and *FA* were the only parameters of DTI metrics that showed significant correlation with aging, exhibiting mostly a negative association. $D_{//}$ tended to decrease with aging in the cerebral peduncle (CER), while FA presented a decrease in frontal WM. Regarding the parameters obtained using higher b-shells, *MK* showed a negative association, while ODI and ν_{fw} of NODDI positively correlated with aging. ν_{in} showed weak
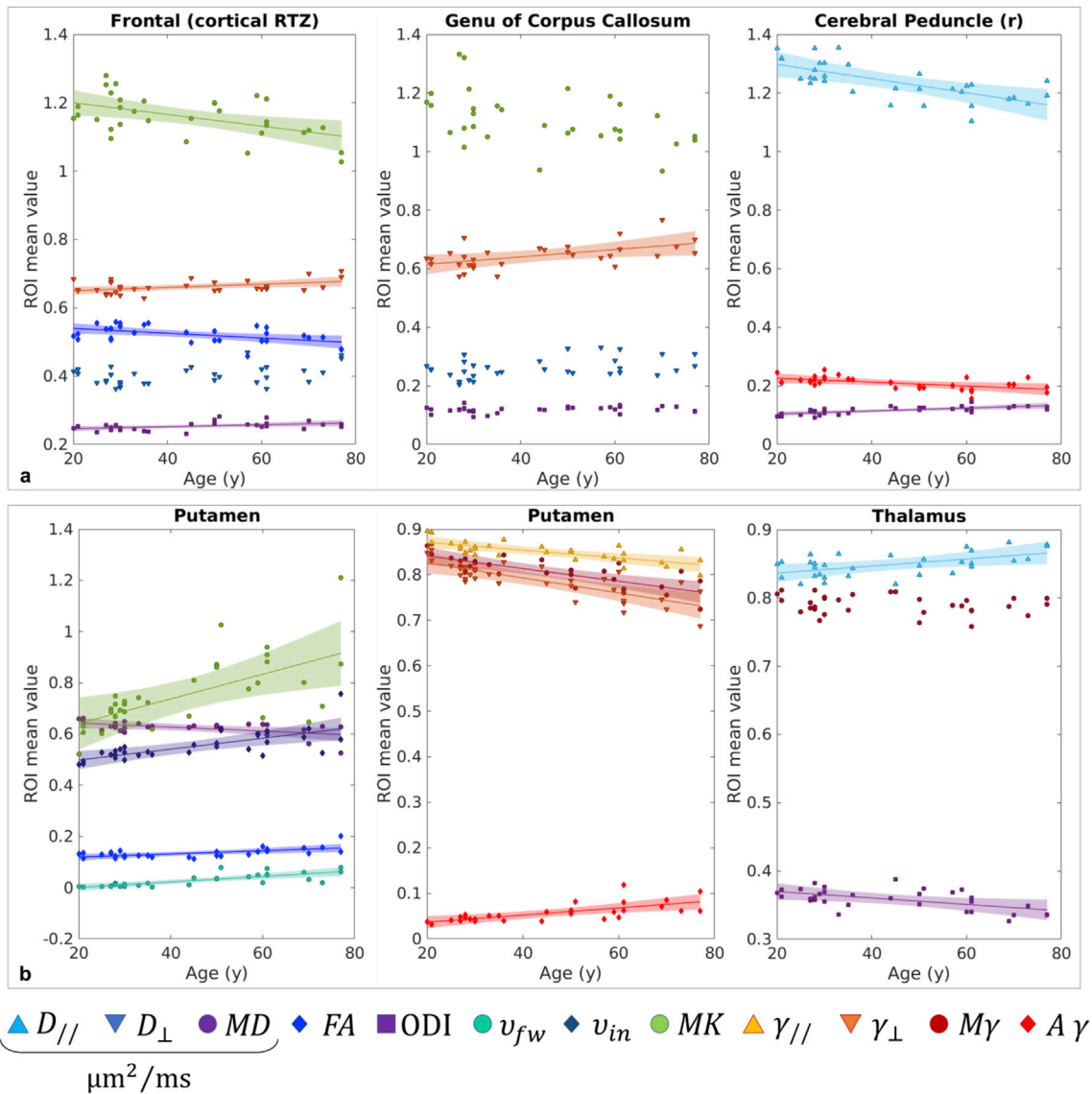
Fig. 4. Plots of different diffusion metrics *vs* age in different regions of WM and scGM. Box *a* shows the trends in WM: the frontal part of the cortical RTZs, the left cerebral peduncle (CER (*l*)) and the genu of corpus callosum (GCC) are reported. Box *b* shows the trends in scGM. The trends within the putamen and the thalamus are reported. On the top-right panel the markers and colors identifying the different parameters. Solid lines are reported where a statistical significance was found ($p_{fwe} <$ 0.05.) The shaded area represents the confidence interval of 95%.

negative trends within the genu of corpus callosum (GCC) and the left anterior corona radiata (CR_A (*l*)) but a positive trend in the left fornix stria terminalis (FOR_C (*l*)).

All γ metrics showed at least one significant correlation. $\gamma_{//}$, $\gamma_\perp$ and $M\gamma$ generally increased although $\gamma_{//}$ and $M\gamma$ showed a decrease in the left retrolenticular part of the internal capsule (IC_R (*l*)) and right sagittal striatum (SS (*r*)). On the other hand, γA generally decreased with advancing age (see Figs. 3 and 4).

As regard the global WM atlas, ODI and MK were the only parameters showing a significant trend. The MK decrease seemed to be driven by a decrease within the cortical RTZs rather than in the core tracts. In particular, the tracts close to the frontal lobe showed the greatest number of significant differences. FA and MK decreased while ODI, $\gamma_\perp$ and $M\gamma$ increased. MK decreased also in the tracts close to the sensory-motor lobe along with a parallel increase in $\gamma_{//}$. No general trends related to core tracts were observed, however several region-specific trends were recognized within the parcellation. On average, the regions showing the strongest correlation were the left and right sides of the CER. Here, a simultaneous decrease in $D_{//}$ and increase in ODI were observed. Also, a

significantly decreased anisotropy in γ was observed. The same pattern of decreased axial diffusivity and increased ODI applied also to both sides of the internal capsule (IC_P), although not statistically significant. γ-derived parameters showed a rather strong correlation within the GCC and (CR_A (*l*)). Among these metrics, $\gamma_\perp$ seemed to be the driving one inducing an increase in $M\gamma$ and a decrease in γA. A positive association was found in the left external capsule between ν_{fw} and age. As regards MK, several negative trends were observed within the core tracts, but none of them were strong enough to be considered significant.

3.1.2. Results in subcortical GM

Besides a few cases, a complete inversion of age-related trends was observed for all the parameters in the sub-cortical regions (Fig. 3): $D_\perp$, MD, ODI, $\gamma_{//}$, $\gamma_\perp$ and $M\gamma$ showed a decrease, whereas FA, ν_{in}, ν_{fw}, γA showed an increase with age. $D_{//}$ showed a positive and negative association with age in the thalamus and in the putamen, respectively. The putamen was with no doubt the region showing the most widespread and strongest correlation with diffusion derived parameters (*i.e.* all apart from ODI). The thalamus showed a pattern similar to that of the CER, but

inverted, *i.e.* increased $D_{//}$ and decreased ODI. Finally, the caudate showed a parallel increase in ν_{in} and ν_{fw} with aging.

3.2. Voxel-wise analysis

The results of the voxel-wise approach were coherent with those found using the ROI-based approach. Regional differences in WM are displayed in Fig. 5. $D_{//}$ and ODI showed mono-lateral differences in the left cerebral peduncle and in the left posterior limb of the internal capsule. This result might highlight a possible associated variation of $D_{//}$ and ODI (Billiet et al., 2015). A general increase in $M\gamma$ and $\gamma_\perp$ vs age was also highlighted (Fig. 5). The effects were widespread in the left frontal area, including the left corona radiata and part of the genu of corpus callosum. In accordance with the results found in the ROI-based analysis, ν_{in} showed a significant increase within the right external capsule. No significant association between MK and age was found in the WM voxel-wise analysis.

Fig. 6 shows the trends of the conventional DTI-parameters and NODDI-parameters in scGM. In the putamen, a decrease in MD together with an increase in FA, ν_{in} and ν_{fw} were observed. ν_{in} increased also in the caudate, while an increase in ν_{fw} was observed in the posterior part of the thalamus. ODI decreased in the thalamus with a spotty pattern. The voxel-wise correlations of γ-derived metrics vs age in scGM are highlighted in Fig. 7. The strong increase in $M\gamma$ and decrease in γA seemed to be driven by a variation in $\gamma_\perp$, rather than $\gamma_{//}$.
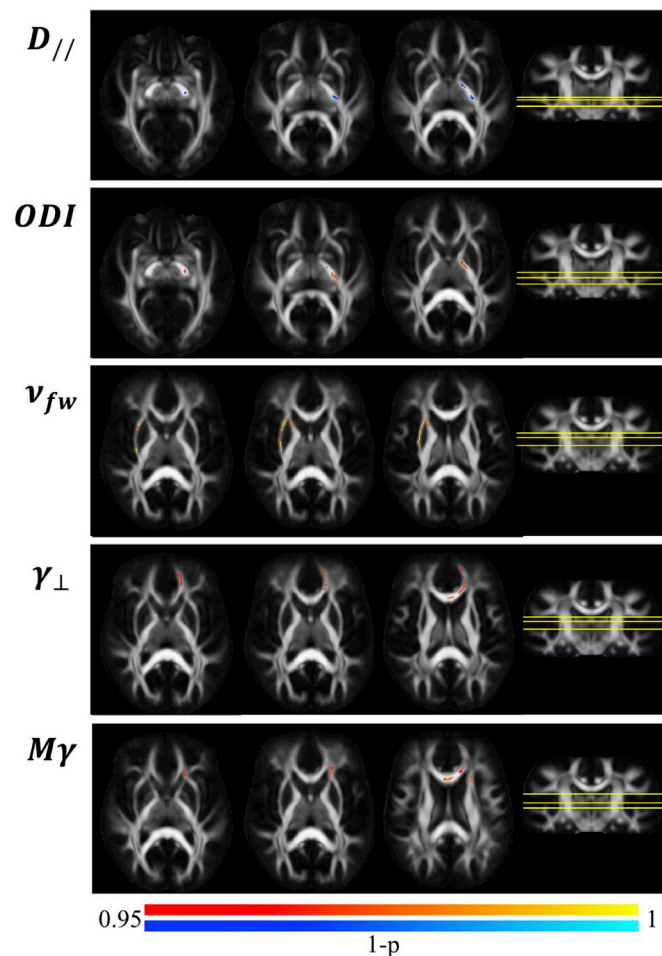
Fig. 5. Results of the voxel-wise analysis of DTI-, NODDI- and γ-metrics correlation with subjects' age in WM. The maps show the corrected p-value $(1-p)$ superimposed on the population specific *FA* template. The red-yellow colors denote positive correlation, while the blue-cyan colors denote negative correlation.
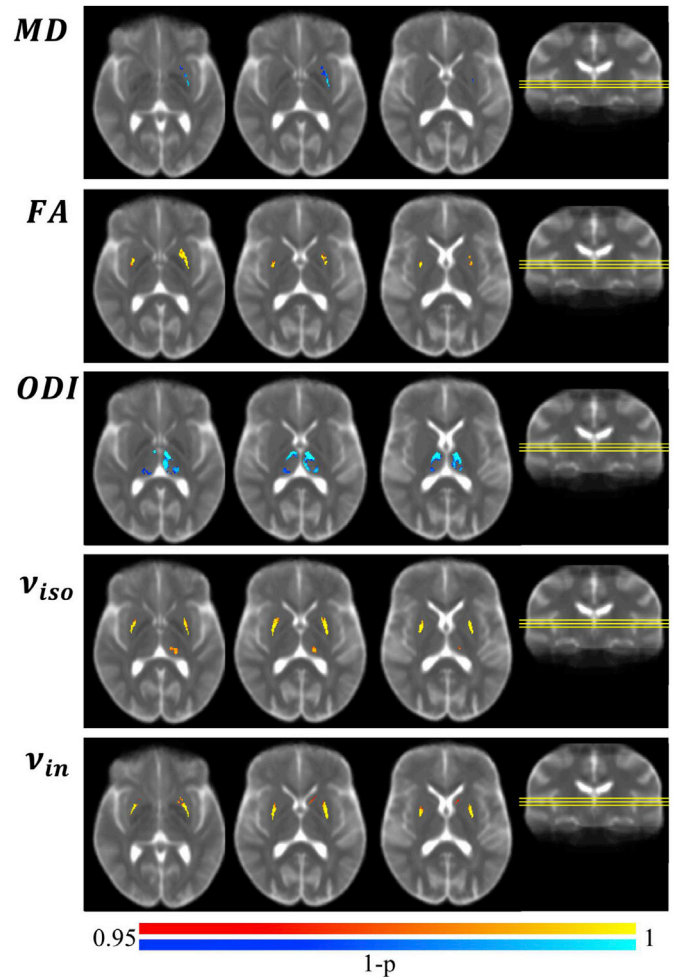
Fig. 6. Results of the voxel-wise analysis of correlation between DTI- and NODDI-derived parameters and subjects' age in scGM. Here the results are superimposed on *MD* population specific template. The red-yellow colors denote a positive correlation, while the blue-cyan colors denote a negative correlation.

3.3. Correlation between metrics

The squared values of linear cross-correlation coefficients calculated between metrics both in total WM and total scGM are displayed in Fig. 8. These values represent the amount of variance that each metrics shares with the others, giving an estimate of how unique the information provided by each metrics is. As expected, the variance shared by parameters derived from the same metrics was high. In WM, $D_\perp$ seemed to account for most of the variability of FA and MD. ν_{in} shared a large portion of variance with all the DTI parameters and specifically with MD and $D_\perp$, while ODI had a negative association with $D_{//}$. MK shared a rather high portion of variance with MD, FA, and $D_\perp$. γ-derived parameters have a rather small portion of variance shared with the other diffusion metrics. The only exception is $\gamma_{//}$ that showed a stronger association with MD, FA and MK.

The right side of Fig. 8 shows the results for scGM. The results appeared to be clustered in a different way. MD and FA on the one hand and $M\gamma$ and γA on the other, shared a large proportion of variance with $D_\perp$ and $\gamma_\perp$, respectively. ODI measure showed a negative correlation only with $D_{//}$ and FA. All the metrics obtained using higher b-shell seemed to share a larger portion of variance. In particular, ν_{in} and ν_{fw} showed a much higher association with γ-metrics, compared to that shown in WM.

Fig. 7. Results of the voxel-wise analysis of correlation between γ-metrics and subjects' age in scGM. The results are superimposed on *MD* population template. The red-yellow colors denote a positive correlation, while the blue-cyan colors denote a negative correlation.

4. Discussion

In this cross-sectional study we assessed the potential of a combined use of γ-metrics and other more widespread diffusion MRI (dMRI) techniques in detecting the microstructural and physiological changes due to normal aging in WM and scGM of the human brain. Previous works (Caporale et al., 2017) highlighted how γ-metrics may reflect inhomogeneities due to Δχ among various tissues and compartments, being potentially useful as an indirect measure of myelin integrity and iron content. In this paper, the cohort of volunteers spanned from young adults to elderly subjects. To analyze the different regions of the brain, we used a hierarchical ROI-based approach in parallel with a voxel-wise-based approach, both in WM and scGM. We found diversified patterns of parameter modifications with advancing age, both in scGM and WM, possibly indicating regional-specific aging processes. The results suggest that γ-metrics is complementary to DTI, DKI and NODDI, highlighting changes not significantly detected by the other conventional metrics.

4.1. Microstructural changes in white matter

The results of this study suggest that a combination of different dMRI-derived techniques permits observation of microscopically different aging patterns within the WM fibers.

The aging of WM fibers appears to be driven by two principal mechanisms: the degradation of nerve fibers and the degeneracy of the myelin (Peters, 2009; Peters and Kemper, 2012). On one hand, degenerating nerve fibers start to accumulate mixtures of organelles and neurofilaments. These accumulations are often related to dystrophy of the axons such as swelling. The degeneration process ends with the complete disintegration of the axon. The extent of lost fibers, in some specific regions of rhesus monkeys' brains, has been quantified to be around 20% in the genu of corpus callosum, 30% in the splenium of corpus callosum and 40% in the anterior commissure (Sandell and Peters, 2003; Bowley et al., 2010). On the other hand, myelin undergoes segmental demyelination that is often followed by remyelination and sometimes by myelin decompaction. Remyelinated segments are thinner and shorter, while decompaction is principally caused by splitting of myelin in the major dense line (Peters, 2009; Peters and Kemper, 2012; Sandell and Peters, 2003; Bowley et al., 2010).

dMRI has been extensively used with the aim to track these microscopic changes in vivo. A large number of cross-sectional studies (Pfefferbaum et al., 2000; Abe et al., 2002; Salat et al., 2005; Sullivan et al., 2010; Ardekani et al., 2007; Giorgio et al., 2010), but also longitudinal studies (Barrick et al., 2010) reported an increase in MD and a decrease in FA. Specifically, FA modifications seem to be mostly related to grater $D_\perp$ rather than $D_{//}$ (Zhang et al., 2010; Bartzokis et al., 2012), suggesting that the FA reductions are linked to myelin degradation and axonal loss. However, some authors pointed out that care should be taken when interpreting these results (Wheeler-Kingshott and Cercignani, 2009).

MK has been shown to decrease with aging (Lätt et al., 2013; Gong et al., 2014; Coutu et al., 2014) indicating a less complex organization of tissues in elderly brains. However, Billet et al. (2015) reported contrasting results showing an increased MK with ageing. However, the investigated age-range was narrower compared to the population studied by the above-mentioned authors.

Few studies reported the association between NODDI parameters and aging (Billet et al., 2015; Cox et al., 2016). ν_{fw} was observed to decrease in both studies, while contradictory results were reported for ν_{in} and ODI: Billet et al. reported an increase in both these parameters, while Cox et al. reported a decrease in both cases. However, the two studies dealt with different age ranges. In a study carried out on a cohort of young to middle-aged adults, (Kodiweera et al., 2016) reported an increase in ODI with aging and observed how this parameter was the most sensitive to microstructural changes compared to DTI parameters.

In order to explain the overall trends of age-related microscopic

Fig. 8. The shared variance between diffusion metrics is displayed separately for white matter (WM), on the left, and subcortical gray matter (scGM), on the right. The higher the reported value, the higher the similarity of the information provided by the two metrics. Warm colors show positive correlation, cold colors represent negative correlation. Significant correlation, corrected for family-wise errors, are highlighted in bold and by a box with dashed contours.

changes, several neurodegenerative theories have been proposed in the past years. For example, it has been established that age-related modifications occur with frontal predominance (Abe et al., 2002; Salat et al., 2005; Ardekani et al., 2007; Sullivan et al., 2010), thus an anterior-posterior gradient of degeneration has been proposed (Sullivan and Pfefferbaum, 2006). On the other hand, according to the retrogensis theory, demyelination is the major driving mechanism of degeneration and the late myelinating fibers are more affected than the early myelinating ones (Stricker et al., 2009; Cox et al., 2016). Finally, the Wallerian degeneration theory proposes that axonal degradation is the result of injuries happening further from the degradation site (Damoiseaux et al., 2009; Davis et al., 2009).

4.1.1. Is γ-imaging sensitive to myelin degradation?

In the past years, *in vitro, ex vivo* and in vivo experiments were performed to investigate the features of the so called pseudo-superdiffusion γ parameter (Palombo et al. 2011, 2012; Capuani et al., 2013; Caporale et al., 2017). The experiments coherently showed that γ quantifies water molecules diffusing with a wide distribution of diffusion lengths in heterogeneous and multi-scale tissues. The width of this set of diffusion lengths is partially due to water diffusion compartmentalization, but also to the inhomogeneity (or averaged internal gradients g_{int}) coming from local $\Delta\chi$ between compartments. In the human brain, $\Delta\chi$ arises from differences in non-heme iron contents and iron-storage proteins and from various degrees of myelin density and orientation with respect to B_0. It has been found that γ values decreased in parallel to $\Delta\chi$-derived g_{int} increase (Palombo et al. 2011, 2012; Capuani et al., 2013; Caporale et al., 2017). Moreover, by repeating the γ-imaging studies in the brain of distinct groups of healthy subjects, using acquisitions obtained with a different number of diffusion gradient directions, we found an excellent agreement between the mean γ values representative of certain brain regions (De Santis et al., 2011; GadElkarim et al., 2013; Caporale et al., 2017).

Our results showed a significant increase in $\gamma_\perp$ as a function of age in frontal WM and more specifically in the genu of corpus callosum and anterior corona radiata (Figs. 3 and 5). We suggest that these results which are in agreement with our previous findings (Caporale et al., 2017), might reflect an effective decrease in the thickness and integrity of the myelin sheaths across the densely packed WM fibers. Indeed a reduction of myelin would affect the g_{int} between the myelinated axons to which γ parameters are sensitive, in at least two ways: first, decreasing the value of the magnetic susceptibility of axons compared to that of the surrounding tissues and thus inducing a decreased $\Delta\chi$; second, inducing a more prominent averaging effect of the diffusion on the inhomogeneities induced by $\Delta\chi$ by increasing the space between the axons (Mitchell et al., 2010; Di Pietro et al., 2014). The overall effect would thus be a decrease in the magnitude of internal gradients g_{int} with a consequent increase in γ.

Our speculations may be supported by other studies using different MRI techniques. For example, the decrease in magnetization transfer (MT) is associated with loss of macromolecular content, typically myelin. Two different studies (Draganski et al., 2011; Callaghan et al., 2014) using a quantitative MT approach to study brain aging, showed regional patterns of decreased MT similar to those observed in our voxel-wise analysis of $M\gamma$ and $\gamma_\perp$.

Neither kurtosis nor DTI, and NODDI metrics showed significant correlations with age within the genu and the anterior corona radiata, suggesting the complementarity of the γ metrics compared to the other dMRI metrics in these regions.

4.1.2. ODI increase and $D_{//}$ associated to axonal loss

The present study also found a significant age-related decrease in $D_{//}$ as well as an increase in ODI within the cerebral peduncle (CER), bilaterally, on a ROI-based analysis. The same significant trends were found in the voxel-based analysis within the left CER and left IC_P. Other studies using a TBSS approach on DTI-derived maps reported similar

correlations of $D_{//}$ in the IC_P (Kawaguchi et al., 2010) and both in the CER and the IC_P (Burzynska et al., 2010). In a study using both NODDI and standard DTI metrics, (Billiet et al., 2015) reported a similar pattern of decreased $D_{//}$ and an increased ODI with aging in these regions. However, this decrease was not statistically significant.

This pattern of changes could reflect microscopic aging processes different from those described in the previous section. However, in order to form a hypothesis about the microscopic modifications causing these parameter changes, it is useful to understand the anatomical composition of the IC_P and the CER. These regions are mainly formed by three fiber tracts: the corticospinal, the corticobulbar and the corticopontine. These tracts are components of the projection fibers interconnecting cortical areas with deep nuclei, brain stem, cerebellum and spinal cord. They originate in the cerebral cortex and converge through the corona radiata to form the IC_P in a tightly compact bundle, oriented in a superior-inferior direction. Subsequently, the fibers enter the cerebral peduncle and continue their ways toward different destinations (Jellison et al., 2004). Supposing that the projection fibers are markedly affected by aging, a lowered axial diffusivity may be explained by axonal degeneration processes. Indeed, the beginning of the degeneration is characterized by accumulation of organelles, such as lysosomes and mitochondria, as well as an increase in neurofilament density within the axoplasm, thus hindering water molecule diffusion along the axons (Peters, 2009; Peters and Kemper, 2012). Furthermore, the axons undergo dystrophic changes such as swelling and beading, which have been shown to induce a reduction in $D_{//}$ (Budde and Frank, 2010; Palombo et al., 2017). The space left empty by damaged fibers would thus be occupied by crossing fibers less affected by aging, such as the fibers of the pontocerebellar tract in the cerebral peduncle (Kamali et al., 2010) and those of the corticothalamic tract in the IC_P (Axer and v Keyserlingk, 2000), thus contributing to a decrease in axial diffusivity and explaining the parallel increase in orientation dispersion.

4.1.3. WM modifications in the context of neurodegenerative theories

The results obtained in the cortical RTZs as well as those obtained in the genu of corpus callosum and the corona radiata are in line with the hypothesis of posterior-anterior gradient of degeneration. The greatest correlation between parameters and age was found near the frontal lobe of the cortical RTZs. The decrease in FA, and MK in frontal WM as well as the increase in ODI were coherent with previous studies and the complementary increase in $M\gamma$ and $\gamma_\perp$ with aging well fit a scenario of decreased microstructural complexity, driven by axonal loss and demyelination.

The results obtained in the CER and the IC_P were coherent with the Wallerian hypothesis suggesting that axonal degradation can contribute to the overall degenerating age-related process.

Neither our results nor the interpretations that we proposed are in open contradiction with the retrogenesis hypothesis. The genu is known to myelinate later than other fibers, while the CER and the IC_P that are early myelinating fibers (Kinney et al., 1988), undergo a degeneration process different from demyelination.

4.2. Microstructural variations in subcortical gray matter

In scGM structures we observed a not uniform pattern of parametric correlation with aging, possibly revealing regional-specific microscopic modifications.

4.2.1. The putamen

From a microscopic point of view, the putamen has a relatively simple structure. It is composed by neurons with a thickly spherical arborization, which is densely covered with dendritic spines (Yelnik, 2002). Nonetheless, in this region we found the strongest association between parameters and age. All parameters correlated with age, apart from ODI: MD, axial and radial diffusivity as well as $M\gamma$, axial and radial γ decreased, whereas all the other metrics increased. These results were in

general agreement with those reported in literature. The increase in FA associated with a decrease in MD has been reported (Bhagat and Beaulieu, 2004; Abe et al., 2008; Pfefferbaum et al., 2010; Xu et al., 2015). Specifically, the increase in FA has been associated with a higher decrease in $D_\perp$, compared with a more preserved value of $D_{//}$ (Wang et al., 2010). However, the microscopic changes that drive these parameter modifications are still unclear. Some authors observed how they could be related to the volume reduction of the striatum, with concurrent gliosis and tissue compaction (Wang et al., 2010). Other authors argued that iron deposition may significantly affect the measurement of water diffusion in the brain (Pfefferbaum et al., 2010; Xu et al., 2015). Indeed, it is well established that a progressive iron deposition selectively affects scGM (Hallgren and Sourander, 1958; Schipper, 2004; Acosta-Cabronero et al., 2016) and that the putamen presents the strongest age-related increase (Acosta-Cabronero et al., 2016).

Our recent study of healthy young human brain (Caporale et al., 2017) suggested that γ-metrics is sensitive to non-heme iron concentration, especially in sub-cortical GM. The results obtained in scGM reported in the present study, are in good agreement with these previous findings. Indeed, the marked negative trend of $M\gamma$, $\gamma_{//}$ and $\gamma_\perp$ as a function of age in the putamen may reflect an increasing effect of susceptibility inhomogeneities due to age-related iron accumulation.

According to the literature, an age-related increase in MK within the putamen has been found (Gong et al., 2014). Dependence of the DKI derived metrics on the magnetic field inhomogeneities has already been pointed out (Palombo et al., 2015), so it is likely that the correlation found between the metrics derived by fitting data from the higher b-shells and aging were influenced by the iron deposition. This was corroborated also by the observation that the shared variance between metrics changes when considering WM and scGM. Specifically, in the latter case there was an increase in the variance shared by metrics obtained from the higher b-shells, whereas there was a loss of shared variance between DTI metrics and the others. γ metrics showed a higher correlation with age compared to MK, this was likely due to the higher b-values used. These metrics are likely to be more sensitive to iron deposition. It remains to be understood to what extent these changes are influenced by microscopic changes and to what extent they are caused by local changes in the internal gradient. More studies are required to clarify this issue.

4.2.2. The thalamus

The thalamus is the center through which patterns of nerve tracts from cerebral cortex and subcortical and cerebellar regions connect. From a cytoarchitectonical point of view, it is divided into numerous nuclei, each of which reflects a different functional connection with the cortex. Several studies have reported a generalized age-related volume decrease (Raz et al., 2005; Cherubini et al., 2009; Hughes et al., 2012), and it has been observed that some of the subregions undergo differential shape changes with aging, including the anterior, the ventroanterior and the dorsomedial nuclei (Hughes et al., 2012). DTI studies have reported an increase in MD along with a non-significant decrease in FA using both a ROI-based (Cherubini et al., 2009; Hughes et al., 2012; Gong et al., 2014) and a voxel-based approach (Draganski et al., 2011). Also, Gong et al. observed a decrease in MK (Gong et al., 2014), but there is no study assessing the association between NODDI parameters and age within the thalamus in the literature. Our results did not highlight MK correlation with age, while they showed a decreased orientation dispersion using both the ROI-based and the voxelwise-based approach as well as an increased axial diffusivity only in the ROI-based approach. The voxelwise results showed a bilateral pattern of ODI increase that is more accentuated in the left thalamus. The most affected regions seemed to be the ventro-lateral and ventro-anterior nuclei belonging to the so-called lateral group as well as some nuclei of the medial group such as the center median and parafascicular groups, as defined by Morel et al. Microscopically these regions are characterized by a higher concentration of myelinated fibers (Morel et al., 1997; Danos et al., 2003). It has

been established that, with aging, the dendritic tree undergoes a progressive regression in GM, implying the reduction in number and length of the branches and the decrease in the number of spines (Scheibel et al., 1975; Nakamura et al., 1985; Dumitriu et al., 2010). In a recent study, comparing histology derived parameters and NODDI derived parameters on spinal cord lesions from patients with multiple sclerosis, it has been shown that ODI well matched its histology counterpart and, furthermore, that a lower ODI in the lesions was indicative of reduced neurite architecture complexity (Grussu et al., 2017). Thus, regression of the dendritic tree combined with relatively unaffected thalamic fibers would cause reduced neurite dispersion as well as increased axial diffusivity, since the extra axonal water would be less hindered along the direction of the fibers. Another possible explanation could be a selective degradation of some fiber bundles.

4.3. Interpretation of the NODDI parameter modifications with aging

We found several associations between NODDI parameters and aging in different brain regions. However, the interpretation of this correlation could be tricky. A recent study showed that some NODDI constraints seem to be invalid (Lampinen et al., 2017). This inconsistency does not hinder the model from fitting the data, especially in WM and thus the reported associations are thought to be reliable. However, the interpretations of the parameters could be misleading. This should be particularly true for the ν_{in} and ν_{fw} parameters, while ODI is supposed to be negligibly affected (Zhang et al., 2012; Lampinen et al., 2017).

4.4. Methodological considerations

Although the studied cohort of subjects covered a broad age range, the total number of volunteers recruited for the present study was smaller compared to other studies focused on aging (Callaghan et al., 2014; Gong et al., 2014; Billet et al., 2015; Cox et al., 2016; Kodiweera et al., 2016). However, our findings related to DTI, NODDI and MK metrics are broadly in accordance with those presented in previous studies of larger cohorts (Billet et al., 2015; Kodiweera et al., 2016; Gong et al., 2014).

In this study we assessed association between diffusion metrics and aging using a simple linear regression. Other similar studies suggested that age-related changes follow non-linear trajectories (Billet et al., 2015; Cox et al., 2016). However strong deviations from linear trends have been primarily observed in different age ranges such as in brain maturation (Chang et al., 2015) or including elderly subjects (Cox et al., 2016). Moreover, we found that linear regression well described the trends observed in our data. Further studies involving more and older subjects, (>60y) are needed to investigate higher order differences of γ-metrics with age.

Inadequate signal to noise ratio (SNR) can bias diffusion parameter estimation. To validate the reliability of the quantified metrics, we investigated the SNR of our raw DW data as a function of the b-values in WM and scGM (supplementary materials). We found that SNR was above the critical value SNR = 3. This should ensure an unbiased quantification of the diffusion metrics obtained using higher b-values (Caporale et al., 2017, Jones et al., 2013).

Despite the quantification of γ-metrics requires the acquisition of images with b values higher than those used to obtain DTI, DKI and NODDI metrics, the γ-metrics maps seem to be characterized by a lower contrast to noise ratio than the maps reconstructed with the other metrics. This could affect the accuracy and sensitivity of the technique. However, it should be considered that γ-derived maps show a different kind of information compared to that of conventional diffusion methods, which apparently varies less across tissues.

This study suggests the ability of γ-metrics to detect age-related differences due to changes in $\Delta\chi$-driven inhomogeneities. Future studies should corroborate the results of the present study, possibly using other specific quantitative MRI techniques such as quantitative susceptibility mapping (QSM) or magnetization transfer (MT) to compare our

technique with the two most common techniques used for quantification of iron deposition and myelin content.

The long scanning time required by the diffusion protocol used in this study limits the amount of different acquisitions and it is one of the major issues linked to the achievement of γ-weighted maps. Therefore, the use of higher-performance scanners with parallel acquisition mode is necessary to carry out this type of investigation involving multi-b-value acquisitions. In supplementary materials, the results of a preliminary study investigating the feasibility of using a down sampled protocol (with a halved number of b-values and the same number of directions) have been reported. Our preliminary results in supplementary materials showed that a protocol with a higher number of b-acquisitions, such as the one used in this study, helped to reduce the variability in the γ extraction and in the bias introduced when using the DTI reference frame approximation to extract the relevant γ-metrics according to (De Santis et al., 2011). However, the results also showed that by using a reduced number of acquisitions it is still possible to obtain a reliable quantification of γ. Further studies are needed to obtain the best tradeoff between an optimized protocol and reliable maps.

In this study we presented several associations between diffusion metrics and age. These correlations don't necessarily imply a causal relationship. It is possible that other factors, such as technical differences between different metrics, alter the sensitivity or accuracy of the fitting to the data. This could potentially mean that the differences in correlations identified in the results are not necessarily related to the ability of the techniques to identify different ageing mechanisms. Further studies are necessary to confirm the conclusions of the present work.

5. Conclusion

In this study we used DTI, NODDI, MK and γ-metrics to assess physiological (i.e. the iron content) and microstructural (myelin damage, axonal disintegration, neuron cell loss) changes in cerebral WM and scGM of middle- and older-aged subjects. We found that γ-metrics are remarkably sensitive and provide more complementary information than DTI-metrics, MK and NODDI in the detection of frontal changes in the WM. The combined use of these techniques may also reveal different patterns of age-related changes.

This study suggests that an increase in $\gamma_\perp$ values within WM may reflect myelin degradation, and a decrease in Mγ within scGM, specifically in the putamen, may reflect iron deposit accumulations. Changes in $D_{//}$ and ODI could be indices of axon degradation in the pyramidal tract while reflecting decreased architecture complexity within the thalamus. This study demonstrates the added value of γ-metrics for assessing microscopic brain alterations due to aging and providing independent measurements that are complementary to the conventional diffusion metrics. In conclusion, γ-metrics combined with other DW-derived metrics can more comprehensively characterize the complex mechanisms underlying age-related changes than conventional diffusion techniques alone.

Resource data for this article

The data belongs to a larger research project and we are not allowed to share it.

Appendix A. Supplementary data

Supplementary data to this article can be found online at https://doi.org/10.1016/j.neuroimage.2018.12.044.

References

Abe, O., Aoki, S., Hayashi, N., Yamada, H., Kunimatsu, A., Mori, H., Yoshikawa, T., Okubo, T., Ohtomo, K., 2002. Normal aging in the central nervous system: quantitative mr diffusion-tensor analysis. Neurobiol. Aging 23 (3), 433–441.

Abe, O., Yamasue, H., Aoki, S., Suga, M., Yamada, H., Kasai, K., Masutani, Y., Kato, N., Kato, N., Ohtomo, K., 2008. Aging in the cns: comparison of gray/white matter volume and diffusion tensor data. Neurobiol. Aging 29 (1), 102–116.

Acosta-Cabronero, J., Betts, M.J., Cardenas-Blanco, A., Yang, S., Nestor, P.J., 2016. In vivo mri mapping of brain iron deposition across the adult lifespan. J. Neurosci. 36 (2), 364–374.

Andersson, J.L.R., Sotiropoulos, S.N., 2016. An integrated approach to correction for off-resonance effects and subject movement in diffusion MR imaging. NeuroImage 125, 1063–1078, 2016.

Ardekani, S., Kumar, A., Bartzokis, G., Sinha, U., 2007. Exploratory voxel-based analysis of diffusion indices and hemispheric asymmetry in normal aging. Magn. Reson. Imag. 25 (2), 154–167.

Ashraf, A., Clark, M., So, P.-W., 2018. The aging of iron man. Front. Aging Neurosci. 10, 65.

Axer, H., v Keyserlingk, D.G., 2000. Mapping of fiber orientation in human internal capsule by means of polarized light and confocal scanning laser microscopy. J. Neurosci. Methods 94 (2), 165–175.

Barrick, T.R., Charlton, R.A., Clark, C.A., Markus, H.S., 2010. White matter structural decline in normal ageing: a prospective longitudinal study using tract-based spatial statistics. Neuroimage 51 (2), 565–577.

Bartzokis, G., Lu, P.H., Heydari, P., Couvrette, A., Lee, G.J., Kalashyan, G., Freeman, F., Grinstead, J.W., Villablanca, P., Finn, J.P., et al., 2012. Multimodal magnetic resonance imaging assessment of white matter aging trajectories over the lifespan of healthy individuals. Biol. Psychiatry 72 (12), 1026–1034.

Basser, P.J., Mattiello, J., LeBihan, D., 1994. Mr diffusion tensor spectroscopy and imaging. Biophys. J. 66 (1), 259–267.

Bhagat, Y.A., Beaulieu, C., 2004. Diffusion anisotropy in subcortical white matter and cortical gray matter: changes with aging and the role of csf-suppression. J. Magn. Reson. Imag. 20 (2), 216–227.

Billiet, T., Vandenbulcke, M., Mädler, B., Peeters, R., Dhollander, T., Zhang, H., Deprez, S., Van den Bergh, B.R., Sunaert, S., Emsell, L., 2015. Age-related microstructural differences quantified using myelin water imaging and advanced diffusion mri. Neurobiol. Aging 36 (6), 2107–2121.

Bowley, M.P., Cabral, H., Rosene, D.L., Peters, A., 2010. Age changes in myelinated nerve fibers of the cingulate bundle and corpus callosum in the rhesus monkey. J. Comp. Neurol. 518 (15), 3046–3064.

Budde, M.D., Frank, J.A., 2010. Neurite beading is sufficient to decrease the apparent diffusion coefficient after ischemic stroke. Proc. Natl. Acad. Sci. Unit. States Am. 107 (32), 14472–14477.

Burzynska, A.Z., Preuschhof, C., Bäckman, L., Nyberg, L., Li, S.C., Lindenberger, U., Heekeren, H.R., 2010. Age-related differences in white matter microstructure: region-specific patterns of diffusivity. Neuroimage 49 (3), 2104–2112.

Callaghan, M.F., Freund, P., Draganski, B., Anderson, E., Cappelletti, M., Chowdhury, R., Diedrichsen, J., FitzGerald, T.H., Smittenaar, P., Helms, G., et al., 2014. Widespread age-related differences in the human brain microstructure revealed by quantitative magnetic resonance imaging. Neurobiol. Aging 35 (8), 1862–1872.

Caporale, A., Palombo, M., Macaluso, E., Guerreri, M., Bozzali, M., Capuani, S., 2017. The γ-parameter of anomalous diffusion quantified in human brain by mri depends on local magnetic susceptibility differences. Neuroimage 147, 619–631.

Capuani, S., Palombo, M., Gabrielli, A., Orlandi, A., Maraviglia, B., Pastore, F.S., 2013. Spatio-temporal anomalous diffusion imaging: results in controlled phantoms and in excised human meningiomas. Magn. Reson. Imag. 31 (3), 359–365.

Chang, Y.S., Owen, J.P., Pojman, N.J., Thieu, T., Bukshpun, P., Wakahiro, M.L., Berman, J.I., Roberts, T.P., Nagarajan, S.S., Sherr, E.H., et al., 2015. White matter changes of neurite density and fiber orientation dispersion during human brain maturation. PLoS One 10 (6) e0123656.

Cherubini, A., Péran, P., Caltagirone, C., Sabatini, U., Spalletta, G., 2009. Aging of subcortical nuclei: microstructural, mineralization and atrophy modifications measured in vivo using mri. Neuroimage 48 (1), 29–36.

Coutu, J.P., Chen, J.J., Rosas, H.D., Salat, D.H., 2014. Non-Gaussian water diffusion in aging white matter. Neurobiol. Aging 35 (6), 1412–1421.

Cox, S.R., Ritchie, S.J., Tucker-Drob, E.M., Liewald, D.C., Hagenaars, S.P., Davies, G., Wardlaw, J.M., Gale, C.R., Bastin, M.E., Deary, I.J., 2016. Ageing and brain white matter structure in 3,513 UK biobank participants. Nat. Commun. 7, 13629.

Damoiseaux, J.S., Smith, S.M., Witter, M.P., Sanz-Arigita, E.J., Barkhof, F., Scheltens, P.,, et al., 2009. White matter tract integrity in aging and Alzheimer's disease. Hum. Brain Mapp. 30 (4), 1051–1059.

Danos, P., Baumann, B., Krämer, A., Bernstein, H.-G., Stauch, R., Krell, D., Falkai, P., Bogerts, B., 2003. Volumes of association thalamic nuclei in schizophrenia: a postmortem study. Schizophr. Res. 60 (2–3), 141–155.

Daugherty, A.M., Raz, N., 2015. Appraising the role of iron in brain aging and cognition: promises and limitations of mri methods. Neuropsychol. Rev. 25 (3), 272–287.

Davis, S.W., Dennis, N.A., Buchler, N.G., White, L.E., Madden, D.J., Cabeza, R., 2009. Assessing the effects of age on long white matter tracts using diffusion tensor tractography. Neuroimage 46 (2), 530–541.

De Santis, S., Gabrielli, A., Bozzali, M., Maraviglia, B., Macaluso, E., Capuani, S., 2011. Anisotropic anomalous diffusion assessed in the human brain by scalar invariant indices. Magn. Reson. Med. 65 (4), 1043–1052.

Destainville, N., Saulière, A., Salomé, L., 2008. Comment to the article by Michael J. Saxton: a biological interpretation of transient anomalous subdiffusion. I. Qualitative model. Biophys. J. 95, 3117–3119.

Di Pietro, G., Palombo, M., Capuani, S., 2014. Internal magnetic field gradients in heterogeneous porous systems: comparison between spin-echo and diffusion decay internal field (DDIF) method. Appl. Magn. Reson. 45 (8), 771–784.

Draganski, B., Ashburner, J., Hutton, C., Kherif, F., Frackowiak, R.S., Helms, G., Weiskopf, N., 2011. Regional specificity of mri contrast parameter changes in normal ageing revealed by voxel-based quantification (vbq). Neuroimage 55 (4), 1423–1434.

Dumitriu, D., Hao, J., Hara, Y., Kaufmann, J., Janssen, W.G., Lou, W., Rapp, P.R., Morrison, J.H., 2010. Selective changes in thin spine density and morphology in monkey prefrontal cortex correlate with aging-related cognitive impairment. J. Neurosci. 30 (22), 7507–7515.

GadElkarim, J.J., Magin, R.L., Meerschaert, M.M., Capuani, S., Palombo, M., Kumar, A., Leow, A.D., 2013. Fractional order generalization of anomalous diffusion as a multidimensional extension of the transmission line equation. IEEE J. Emerg. Sel. Top. Circ. Syst. 3 (3), 432–441.

Giorgio, A., Santelli, L., Tomassini, V., Bosnell, R., Smith, S., De Stefano, N., Johansen-Berg, H., 2010. Age-related changes in grey and white matter structure throughout adulthood. Neuroimage 51 (3), 943–951.

Gong, N.-J., Wong, C.-S., Chan, C.-C., Leung, L.-M., Chu, Y.-C., 2014. Aging in deep gray matter and white matter revealed by diffusional kurtosis imaging. Neurobiol. Aging 35 (10), 2203–2216.

Grussu, F., Schneider, T., Tur, C., Yates, R.L., Tachrount, M., Ianuş, A., Yiannakas, M.C., Newcombe, J., Zhang, H., Alexander, D.C., et al., 2017. Neurite dispersion: a new marker of multiple sclerosis spinal cord pathology? Ann. Clin. Transl. Neurol. 4 (9), 663–679.

Haacke, E.M., Miao, Y., Liu, M., Habib, C.A., Katkuri, Y., Liu, T., Yang, Z., Lang, Z., Hu, J., Wu, J., 2010. Correlation of putative iron content as represented by changes in r2* and phase with age in deep gray matter of healthy adults. J. Magn. Reson. Imag. 32 (3), 561–576.

Hall, M.G., Barrick, T.R., 2012. Two-step anomalous diffusion tensor imaging. NMR Biomed. 25 (2), 286–294, 210.1002/nbm.1747.

Hallgren, B., Sourander, P., 1958. The effect of age on the nonhaemin iron in the human brain. J. Neurochem. 3 (1), 41–51.

Hansen, B., Lund, T.E., Sangill, R., Jespersen, S.N., 2013. Experimentally and computationally fast method for estimation of a mean kurtosis. Magn. Reson. Med. 69 (6), 1754–1760.

Hughes, E.J., Bond, J., Svrckova, P., Makropoulos, A., Ball, G., Sharp, D.J., Edwards, A.D., Hajnal, J.V., Counsell, S.J., 2012. Regional changes in thalamic shape and volume with increasing age. Neuroimage 63 (3), 1134–1142.

Ingo, C., Magin, R.L., Colon-Perez, L., Triplett, W., Mareci, T.H., 2014. On random walks and entropy in diffusion-weighted magnetic resonance imaging studies of neural tissue. Magn. Reson. Med. 71 (2), 617–627 doi:610.1002/mrm.24706.

Jelescu, I.O., Budde, M.D., 2017. Design and validation of diffusion mri models of white matter. Front. Phys. 5, 61.

Jellison, B.J., Field, A.S., Medow, J., Lazar, M., Salamat, M.S., Alexander, A.L., 2004. Diffusion tensor imaging of cerebral white matter: a pictorial review of physics, fiber tract anatomy, and tumor imaging patterns. Am. J. Neuroradiol. 25 (3), 356–369.

Jensen, J.H., Helpern, J.A., Ramani, A., Lu, H., Kaczynski, K., 2005. Diffusional kurtosis imaging: the quantification of non-Gaussian water diffusion by means of magnetic resonance imaging. Magn. Reson. Med. 53, 1432–1440.

Jones, D.K., Horsfield, M.A., Simmons, A., 1999. Optimal strategies for measuring diffusion in anisotropic systems by magnetic resonance imaging. Magn. Reson. Med. Off. J. Int. Soc. Magn. Reson. Med. 42 (3), 515–525.

Jones, D.K., Knösche, T.R., Turner, R., 2013. White matter integrity, fiber count, and other fallacies: the do's and don'ts of diffusion MRI. Neuroimage 73, 239–254.

Kamali, A., Kramer, L.A., Frye, R.E., Butler, I.J., Hasan, K.M., 2010. Diffusion tensor tractography of the human brain cortico-ponto-cerebellar pathways: a quantitative preliminary study. J. Magn. Reson. Imag. 32 (4), 809–817.

Karaman, M.M., Zhou, X.J., 2018. A fractional motion diffusion model for a twice-refocused spin-echo pulse sequence. NMR in Biomedicine 31 (11), e3960.

Kawaguchi, H., Obata, T., Ota, M., Akine, Y., Ito, H., Ikehira, H., Kanno, I., Suhara, T., 2010. Regional heterogeneity and age-related change in subregions of internal capsule evaluated by diffusion tensor imaging. Brain Res. 1354, 30–39.

Keihaninejad, S., Zhang, H., Ryan, N.S., Malone, I.B., Modat, M., Cardoso, M.J., Cash, D.M., Fox, N.C., Ourselin, S., 2013. An unbiased longitudinal analysis framework for tracking white matter changes using diffusion tensor imaging with application to alzheimer's disease. Neuroimage 72, 153–163.

Kellner, E., Dhital, B., Kiselev, V.G., Reisert, M., 2016. Gibbs-ringing artifact removal based on local subvoxel-shifts. Magn. Reson. Med. 76 (5), 1574–1581.

Kingsley, P.B., 2006. Introduction to diffusion tensor imaging mathematics: Part iii. tensor calculation, noise, simulations, and optimization. Concepts Magn. Reson. 28 (2), 155–179.

Kinney, H.C., Brody, B.A., Kloman, A.S., Gilles, F.H., 1988. Sequence of central nervous system myelination in human infancy: ii. patterns of myelination in autopsied infants. J. Neuropathol. Exp. Neurol. 47 (3), 217–234.

Kiselev, V.G., 2017. Fundamentals of diffusion mri physics. NMR Biomed. 30 (3) e3602.

Kodiweera, C., Alexander, A.L., Harezlak, J., McAllister, T.W., Wu, Y.-C., 2016. Age effects and sex differences in human brain white matter of young to middle-aged adults: a dti, noddi, and q-space study. Neuroimage 128, 180–192.

Lampinen, B., Szczepankiewicz, F., Mårtensson, J., van Westen, D., Sundgren, P.C., Nilsson, M., 2017. Neurite density imaging versus imaging of microscopic anisotropy in diffusion mri: a model comparison using spherical tensor encoding. NeuroImage 147, 517–531.

Landman, B.A., Farrell, J.A., Jones, C.K., Smith, S.A., Prince, J.L., Mori, S., 2007. Effects of diffusion weighting schemes on the reproducibility of dti-derived fractional anisotropy, mean diffusivity, and principal eigenvector measurements at 1.5 t. Neuroimage 36 (4), 1123–1138.

Langkammer, C., Schweser, F., Krebs, N., Deistung, A., Goessler, W., Scheurer, E., Sommer, K., Reishofer, G., Yen, K., Fazekas, F., et al., 2012. Quantitative susceptibility mapping (qsm) as a means to measure brain iron? a post mortem validation study. Neuroimage 62 (3), 1593–1599.

Lätt, J., Nilsson, M., Wirestam, R., Ståhlberg, F., Karlsson, N., Johansson, M.,, et al., 2013. Regional values of diffusional kurtosis estimates in the healthy brain. J. Magn. Reson. Imag. 37 (3), 610–618.

Lin, G., 2015. An effective phase shift diffusion equation method for analysis of PFG normal and fractional diffusions. J. Magn. Reson. 259, 232–240.

Lin, G., 2016. Instantaneous signal attenuation method for analysis of PFG fractional diffusions. J. Magn. Reson. 269, 36–49.

Lin, G., 2018. General PFG signal attenuation expressions for anisotropic anomalous diffusion by modified-Bloch equations. Physica A 497, 86–100.

Liu, C., 2010. Susceptibility tensor imaging. Magn. Reson. Med. Off. J. Int. Soc. Magn. Reson. Med. 63 (6), 1471–1477.

Lockhart, S., DeCarli, C., Fama, R., 2014. Neuroimaging of the Aging Brain: Introduction to the Special Issue of Neuropsychology Review.

Magin, R.L., Abdullah, O., Baleanu, D., Zhou, X.J., 2008. Anomalous diffusion expressed through fractional order differential operators in the Bloch–Torrey equation. J. Magn. Reson. 190 (2), 255–270 doi:210.1016/j.jmr.2007.1011.1007.

Metzler, R., Klafter, J., 2000. The random walk's guide to anomalous diffusion: a fractional dynamics approach. Phys. Rep. 339, 1.

Metzler, R., Jeon, J.-H., Cherstvy, A.G., Barkai, E., 2014. Anomalous diffusion models and their properties: non-stationarity, non-ergodicity, and ageing at the centenary of single particle tracking. Phys. Chem. Chem. Phys. 16, 24128.

Mitchell, J., Chandrasekera, T.C., Johns, M.L., Gladden, L.F., Fordham, E.J., 2010. Nuclear magnetic resonance relaxation and diffusion in the presence of internal gradients: the effect of magnetic field strength. Phys. Rev. 81 (2). Article Number: 026101.

Morel, A., Magnin, M., Jeanmonod, D., 1997. Multiarchitectonic and stereotactic atlas of the human thalamus. J. Comp. Neurol. 387 (4), 588–630.

Mori, S., Oishi, K., Jiang, H., Jiang, L., Li, X., Akhter, K., Hua, K., Faria, A.V., Mahmood, A., Woods, R., et al., 2008. Stereotaxic white matter atlas based on diffusion tensor imaging in an icbm template. Neuroimage 40 (2), 570–582.

Nakamura, I., Akiguchi, I., Kameyama, M., Mizuno, N., 1985. Age-related changes of pyramidal cell basal dendrites in layers iii and v of human motor cortex: a quantitative golgi study. Acta Neuropathol. 65 (3–4), 281–284.

Nicholson, C., 2015. Anomalous diffusion inspires anatomical insights. Biophys. J. 108, 2091–2093.

Novikov, D.S., Kiselev, V.G., Jespersen, S.N., 2018. On modeling. Magn. Reson. Med. 79 (6), 3172–3193.

Palombo, M., Gabrielli, A., De Santis, S., Cametti, C., Ruocco, G., Capuani, S., 2011. Spatio-temporal anomalous diffusion in heterogeneous media by nuclear magnetic resonance. J. Chem. Phys. 135 (3), 034504. doi:034510.031063/034501.3610367.

Palombo, M., Gabrielli, A., De Santis, S., Capuani, S., 2012. The γ parameter of the stretched-exponential model is influenced by internal gradients: validation in phantoms. J. Magn. Reson. 216, 28–36. https://doi.org/10.1016/j.jmr.2011.1012.1023.

Palombo, M., Gentili, S., Bozzali, M., Macaluso, E., Capuani, S., 2015. New insight into the contrast in diffusional kurtosis images: does it depend on magnetic susceptibility? Magn. Reson. Med. 73 (5), 2015–2024.

Palombo, M., Ligneul, C., Hernandez-Garzon, E., Valette, J., 2017. Can we detect the effect of spines and leaflets on the diffusion of brain intracellular metabolites? Neuroimage. https://doi.org/10.1016/j.neuroimage.2017.05.003 (in press).

Peters, A., 2009. The effects of normal aging on myelinated nerve fibers in monkey central nervous system. Front. Neuroanat. 3, 11.

Peters, A., Kemper, T., 2012. A review of the structural alterations in the cerebral hemispheres of the aging rhesus monkey. Neurobiol. Aging 33 (10), 2357–2372.

Pfefferbaum, A., Sullivan, E.V., Hedehus, M., Lim, K.O., Adalsteinsson, E., Moseley, M., 2000. Age-related decline in brain white matter anisotropy measured with spatially corrected echo-planar diffusion tensor imaging. Magn. Reson. Med. Off. J. Int. Soc. Magn. Reson. Med. 44 (2), 259–268.

Pfefferbaum, A., Adalsteinsson, E., Rohlfing, T., Sullivan, E.V., 2010. Diffusion tensor imaging of deep gray matter brain structures: effects of age and iron concentration. Neurobiol. Aging 31 (3), 482–493.

Pirpamer, L., Hofer, E., Gesierich, B., De Guio, F., Freudenberger, P., Seiler, S., Duering, M., Jouvent, E., Duchesnay, E., Dichgans, M., et al., 2016. Determinants of iron accumulation in the normal aging brain. Neurobiol. Aging 43, 149–155.

Rathi, Y., Pasternak, O., Savadjiev, P., Michailovich, O., Bouix, S., Kubicki, M., Westin, C.-F., Makris, N., Shenton, M.E., 2014. Gray matter alterations in early aging: a diffusion magnetic resonance imaging study. Hum. Brain Mapp. 35 (8), 3841–3856.

R Core Team, 2014. R: A Language and Environment for Statistical Computing. R Foundation for Statistical Computing, Vienna, Austria, pp. 3–4. http://www.R-project.org/.

Raz, N., Lindenberger, U., Rodrigue, K.M., Kennedy, K.M., Head, D., Williamson, A., Dahle, C., Gerstorf, D., Acker, J.D., 2005. Regional brain changes in aging healthy adults: general trends, individual differences and modifiers. Cerebr. Cortex 15 (11), 1676–1689.

Salat, D., Tuch, D., Greve, D., Van Der Kouwe, A., Hevelone, N., Zaleta, A., Rosen, B., Fischl, B., Corkin, S., Rosas, H.D., et al., 2005. Age-related alterations in white matter microstructure measured by diffusion tensor imaging. Neurobiol. Aging 26 (8), 1215–1227.

Salminen, L.E., Conturo, T.E., Laidlaw, D.H., Cabeen, R.P., Akbudak, E., Lane, E.M., Heaps, J.M., Bolzenius, J.D., Baker, L.M., Cooley, S., et al., 2016. Regional age differences in gray matter diffusivity among healthy older adults. Brain Imag. Behav. 10 (1), 203–211.

Sandell, J.H., Peters, A., 2003. Disrupted myelin and axon loss in the anterior commissure of the aged rhesus monkey. J. Comp. Neurol. 466 (1), 14–30.

Saxton, M.J., 2008. Response to comment by Destainville et al. Biophys. J. 95, 3120–3122.

Scheibel, M.E., Lindsay, R.D., Tomiyasu, U., Scheibel, A.B., 1975. Progressive dendritic changes in aging human cortex. Exp. Neurol. 47 (3), 392–403.

Schipper, H.M., 2004. Brain iron deposition and the free radical-mitochondrial theory of ageing. Ageing Res. Rev. 3 (3), 265–301.

Simmonds, D.J., Hallquist, M.N., Asato, M., Luna, B., 2014. Developmental stages and sex differences of white matter and behavioral development through adolescence: a longitudinal diffusion tensor imaging (dti) study. Neuroimage 92, 356–368.

Smith, S.M., Jenkinson, M., Johansen-Berg, H., Rueckert, D., Nichols, T.E., Mackay, C.E., Watkins, K.E., Ciccarelli, O., Cader, M.Z., Matthews, P.M., et al., 2006. Tract-based spatial statistics: voxelwise analysis of multi-subject diffusion data. Neuroimage 31 (4), 1487–1505.

Stricker, N.H., Schweinsburg, B.C., Delano-Wood, L., Wierenga, C.E., Bangen, K.J., Haaland, K.Y.,, et al., 2009. Decreased white matter integrity in late-myelinating fiber pathways in Alzheimer's disease supports retrogenesis. Neuroimage 45 (1), 10–16.

Sullivan, E.V., Pfefferbaum, A., 2006. Diffusion tensor imaging and aging. Neurosci. Biobehav. Rev. 30 (6), 749–761.

Sullivan, E.V., Rohlfing, T., Pfefferbaum, A., 2010. Quantitative fiber tracking of lateral and interhemispheric white matter systems in normal aging: relations to timed performance. Neurobiol. Aging 31 (3), 464–481.

Timmers, I., Roebroeck, A., Bastiani, M., Jansma, B., Rubio-Gozalbo, E., Zhang, H., 2016. Assessing microstructural substrates of white matter abnormalities: a comparative study using dti and noddi. PLoS One 11 (12) e0167884.

Tournier, J.-D., Calamante, F., Connelly, A., 2012. Mrtrix: diffusion tractography in crossing fiber regions. Int. J. Imag. Syst. Technol. 22 (1), 53–66.

Veraart, J., Fieremans, E., Novikov, D.S., 2016a. Diffusion mri noise mapping using random matrix theory. Magn. Reson. Med. 76 (5), 1582–1593.

Veraart, J., Novikov, D.S., Christiaens, D., Ades-Aron, B., Sijbers, J., Fieremans, E., 2016b. Denoising of diffusion mri using random matrix theory. Neuroimage 142, 394–406.

Wang, Q., Xu, X., Zhang, M., 2010. Normal aging in the basal ganglia evaluated by eigenvalues of diffusion tensor imaging. Am. J. Neuroradiol. 31 (3), 516–520.

Wang, Y., Gupta, A., Liu, Z., Zhang, H., Escolar, M.L., Gilmore, J.H., Gouttard, S., Fillard, P., Maltbie, E., Gerig, G., et al., 2011. Dti registration in atlas based fiber analysis of infantile krabbe disease. Neuroimage 55 (4), 1577–1586.

Wheeler-Kingshott, C.A., Cercignani, M., 2009. About "axial" and "radial" diffusivities. Magn. Reson. Med. Off. J. Int. Soc. Magn. Reson. Med. 61 (5), 1255–1260.

Xu, X., Wang, Q., Zhang, M., 2008. Age, gender, and hemispheric differences in iron deposition in the human brain: an in vivo mri study. Neuroimage 40 (1), 35–42.

Xu, X., Wang, Q., Zhong, J., Zhang, M., 2015. Iron deposition influences the measurement of water diffusion tensor in the human brain: a combined analysis of diffusion and ironinduced phase changes. Neuroradiology 57 (11), 1169–1178.

Yamada, H., Abe, O., Shizukuishi, T., Kikuta, J., Shinozaki, T., Dezawa, K., Nagano, A., Matsuda, M., Haradome, H., Imamura, Y., 2014. Efficacy of distortion correction on diffusion imaging: comparison of fsl eddy and eddy_correct using 30 and 60 directions diffusion encoding. PLoS One 9 (11) e112411.

Yelnik, J., 2002. Functional anatomy of the basal ganglia. Mov. Disord. 17 (S3).

Yu, Q., Reutens, D., Vegh, V., 2018. Can anomalous diffusion models in magnetic resonance imaging be used to characterise white matter tissue microstructure? Neuroimage. NeuroImage 175, 122–137.

Zhang, H., Yushkevich, P.A., Alexander, D.C., Gee, J.C., 2006. Deformable registration of diffusion tensor mr images with explicit orientation optimization. Med. Image Anal. 10 (5), 764–785.

Zhang, Y., Du, A.-T., Hayasaka, S., Jahng, G.-h., Hlavin, J., Zhan, W., Weiner, M.W., Schuff, N., 2010. Patterns of age-related water diffusion changes in human brain by concordance and discordance analysis. Neurobiol. Aging 31 (11), 1991–2001.

Zhang, H., Schneider, T., Wheeler-Kingshott, C.A., Alexander, D.C., 2012. Noddi: practical in vivo neurite orientation dispersion and density imaging of the human brain. Neuroimage 61 (4), 1000–1016.

Zhou, X.J., Gao, Q., Abdullah, O., Magin, R.L., 2010. Studies of anomalous diffusion in the human brain using fractional order calculus. Magn. Reson. Med. 63 (3), 562–569.

Supplementary materials

1. SNR of diffusion data used to quantify the diffusion metrics
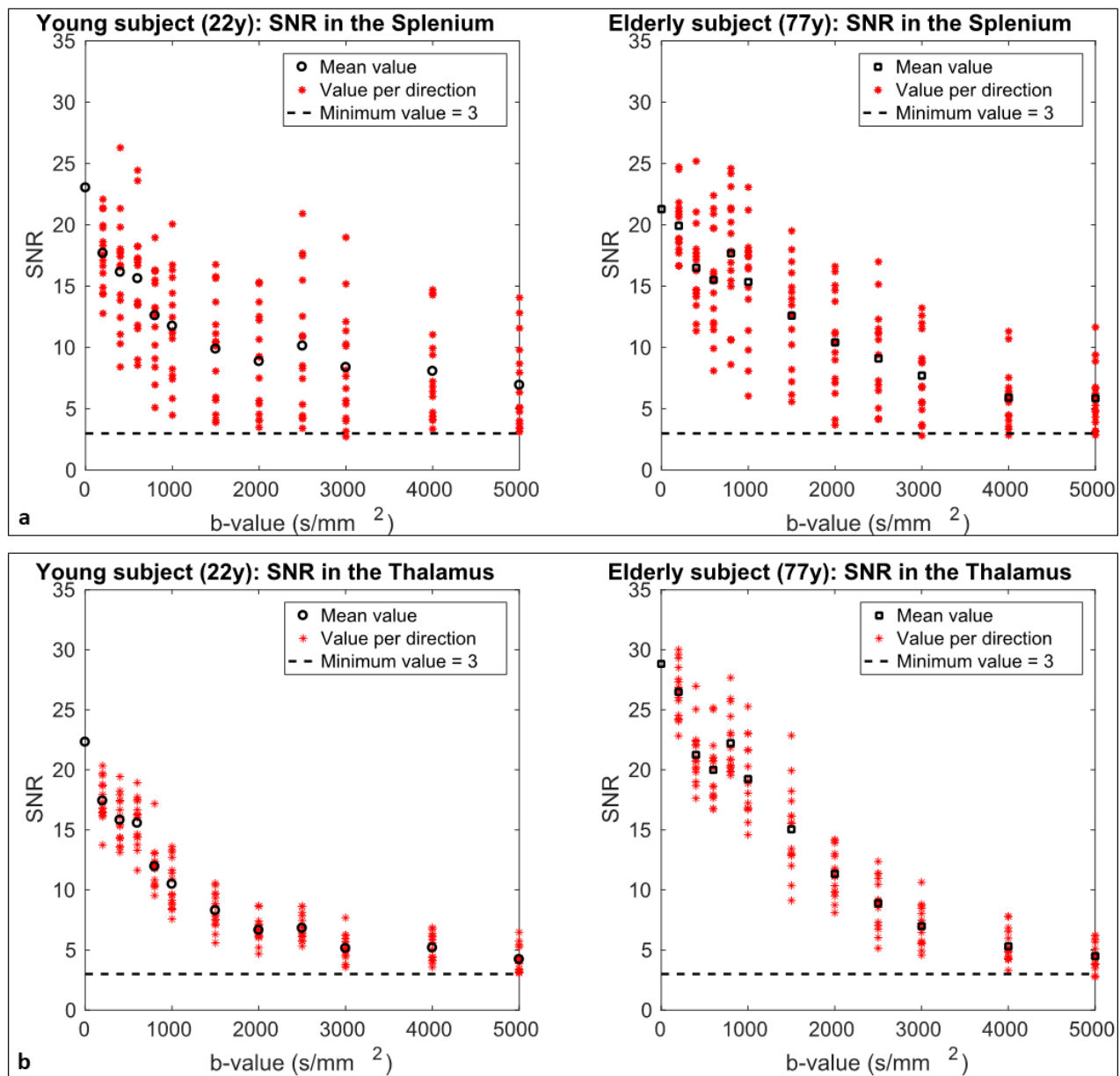
Figure S1: The signal to noise ratio (SNR) of the raw diffusion-data as a function of the b-values. The SNR was calculated with the following formula: $SNR = (m/\sigma)\sqrt{4 - \pi/2}$ (Dietrich, Olaf, et al. *Journal of Magnetic Resonance Imaging* 26.2 (2007): 375-385). m is the mean value of the signal calculated within a foreground region of interest (ROI), σ is the background standard deviation and $\sqrt{4 - \pi/2}$ is a

correction factor to account for the Rayleigh distribution of the noise. We evaluated the SNR in two ROIs: the splenium, representative of highly packed white matter (WM) fibers in box a, and the thalamus, representative of subcortical gray matter (scGM) in box b. Here we report the results for two subjects, one young (22 years) and one elderly (77 years). Each red asterisk denotes the SNR calculated within each acquisition. For each b-value, the 15 red asterisks are associated to acquisitions with different encoding directions. The black circles and black squares are the averaged SNR over the gradient directions. The horizontal black dashed lines in the plots indicate the inferior limit allowed for the reliability of DW data (SNR=3), according to Jones DK *et al.* (Jones DK *et al.*, *Neuroimage,* 73 (2013): 239-254).
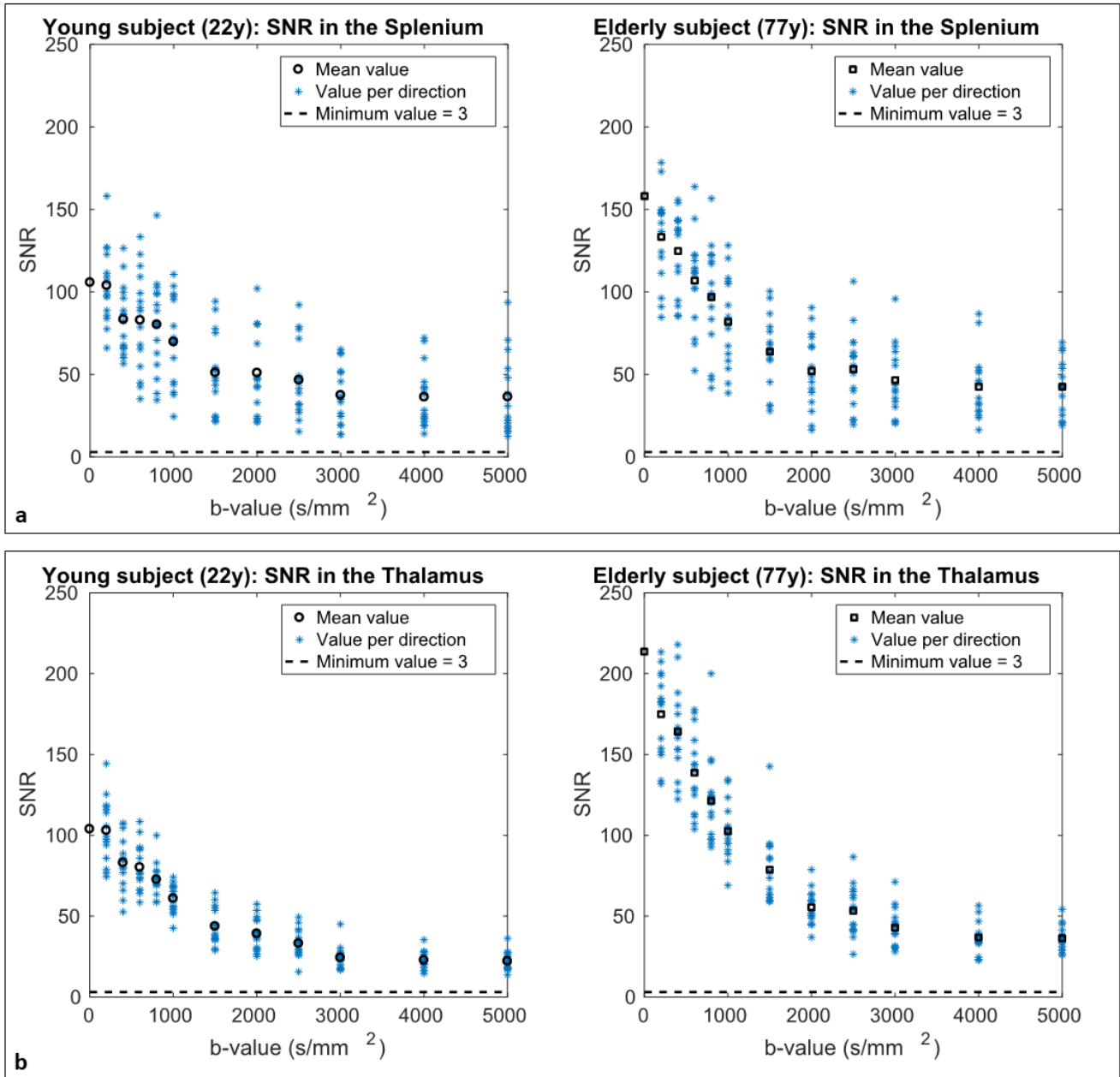
Figure S2: Same as figure S1, but for to the diffusion dataset after de-noising (Veraart, J., Fieremans, E., and Novikov, D. S. (2016a). Diffusion mri noise mapping using random matrix theory. Magnetic resonance in medicine, 76(5):1582–1593. . Here, the SNR was calculated as: $SNR = (m/\sigma)$. The correction factor $\sqrt{4 - \pi/2}$ was discarded since after denoising the noise distribution approaches to a Gaussian distribution. The horizontal black dashed lines in the plots indicate the inferior limit allowed for the reliability of DW data (SNR=3), according to Jones DK et al. (Jones DK et al., Neuroimage, 73 (2013): 239-254).

2. Assessment of the effect of a down sampled acquisition protocol on the estimation of γ parameters

These experiments are meant to test the effect of using a down sampled protocol on estimating γ derived parameters. Also, we used synthetic data to assess the effect on parameter estimation when the assumption that the diffusion tensor and gamma tensor didn't shear the same system of reference.

We generated data using three different subsets of parameters that are summarized in table 1. The data were generated using the same protocol that we used in our work, i.e. 11 b-values ranging from 200 to 5000 s/mm^2. We referred to this protocol as P0 (table 2).

In our analysis we considered five more protocols divided in two sets. The first set included three protocols P1, P2, and P3 with halved number of b-values compared to P0 and same number of directions (table 2). The second set included two protocols (A1 and A2) with only three b-values and same number of directions.

We carried out three experiments, the first two using in silico data, while the third using in vivo data. In the first experiment we assessed the effect that noise has on the parameters estimation when fitting the signal obtained by a known set of parameters. To generate the signal, we used equation number (5) within the manuscript. We used three sets of parameters that are listed in table S1.

In the second experiment, besides adding noise, we intentionally violated the hypothesis whereby DTI and γ-tensor share the same frame of reference. We thus evaluated the effect that this violation has on the parameter estimation.

In the last experiment, using in vivo data from three subject of our cohort, we calculated the γ-metrics using the protocols P1, P2, P3 and assessed the error committed in the estimation of these γ-metrics compared to the "gold standard" obtained with the P0 protocol.

■ Effect of noise in the parameter estimation

We generated the synthetic data and added gaussian noise in quadrature to the signal (so to obtain a SNR for the b_0 equal to 25). We considered 100 realizations for each set of parameters. We fitted the data

using our model (equation (5)) using the down sampled datasets corresponding to each of the six protocols.

Figure S3 shows the results for gamma values. Each column represents a different set of parameters. The black dashed line indicates the true value of each parameter. The markers and the bars are the mean and standard deviation obtained by averaging over the 100 realizations. All the protocols seem to return rather accurate estimates of the parameters, the differences lying principally in the precision.
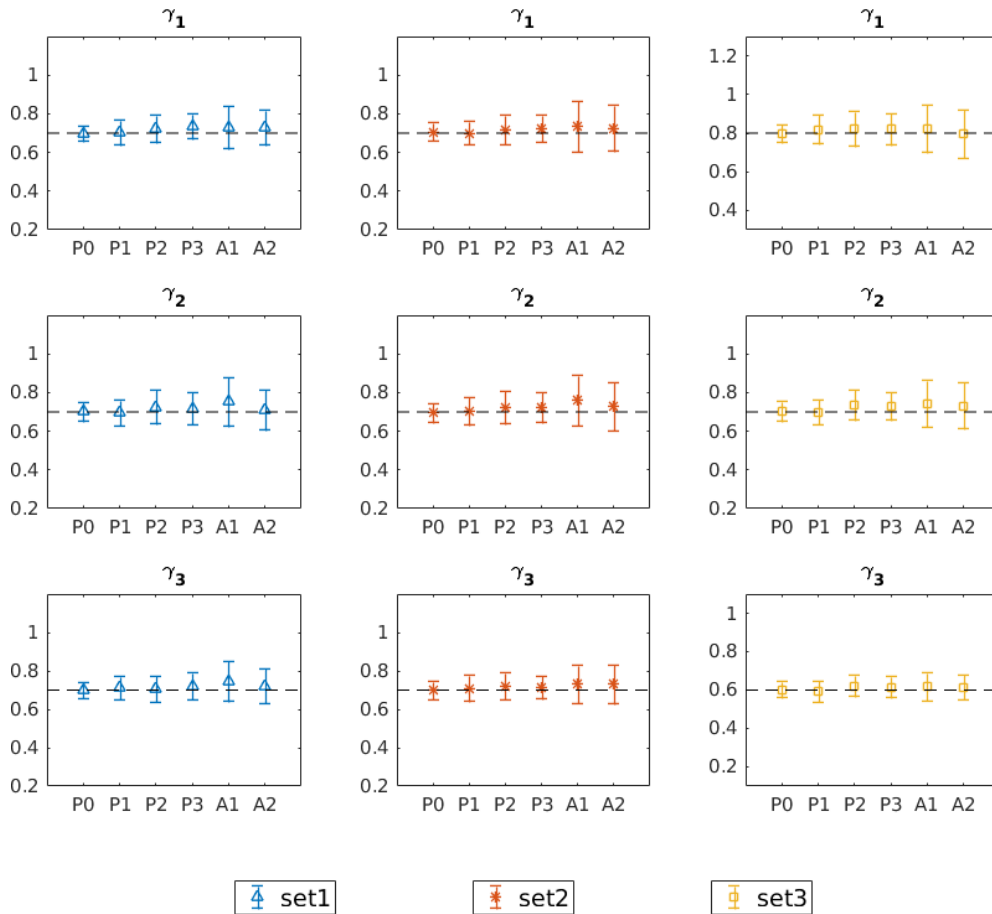
Figure S3: Results of the parameter estimation using different protocols. The columns represent different set of parameters with which the signal was generated. The black dashed indicates the true value of each parameter. The markers and the bars are the mean and standard deviation obtained by averaging over the 100 realizations.

Biases due to not shared system of reference

We repeated the experiment 1), but this time fitting the data with a system of reference intentionally different from the one used to generate the data. This experiment aims to simulate a situation in which

the system of reference of the diffusion tensor and that of the gamma tensor are not the same (see section 2.4.3 within the manuscript). Figure S4 shows the results for this experiment: the quite reach P0 protocol still return a rather accurate estimate of the three parameters for all the three datasets. The parameter estimates made using the down sampled datasets are less accurate and return higher values of the parameters.
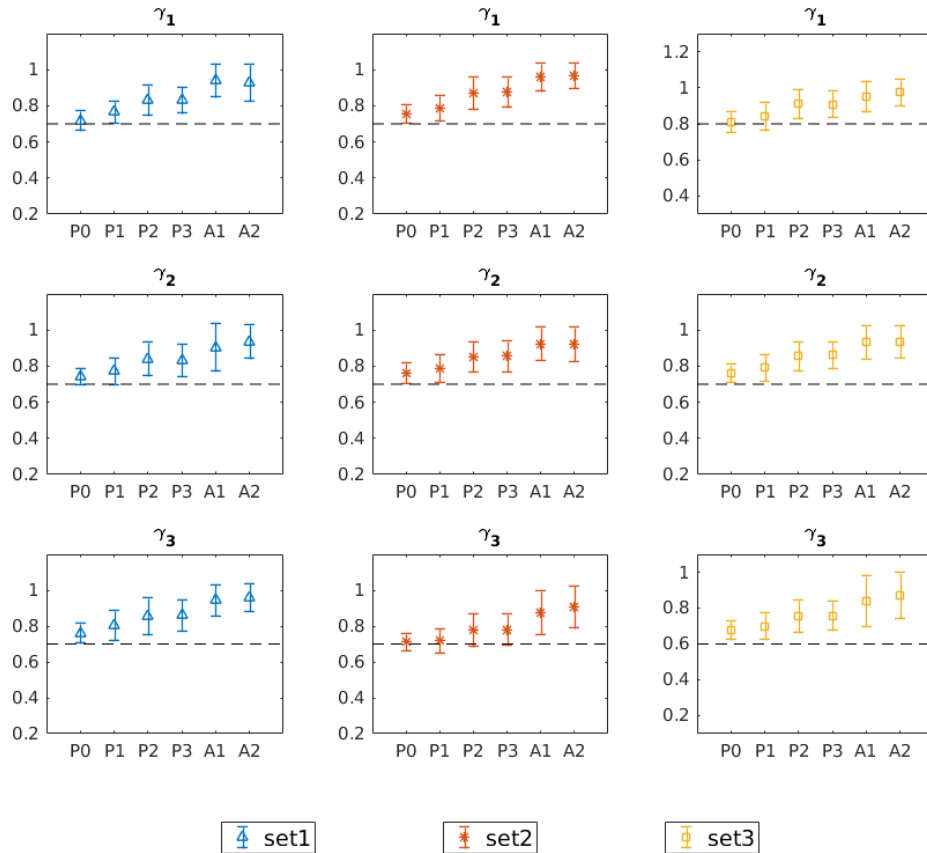
Figure S4: Same as figure S3 but this time, besides the noise, a bias has been intentionally introduced to simulate the situation in which the system of reference of the diffusion tensor and that of the gamma tensor are not shared.

▮ Effect on *in vivo* data

We considered three subjects picked from those used in our study (one young, one adult and one elderly). We fitted our stretched exponential function to three down sampled datasets corresponding to the P1 P2 and P3 protocols and calculated the gamma metrics (mean γ (Mγ), γ anisotropy (γA), axial γ (γ//) and radial γ (γ⊥)).

By considering the values obtained by fitting the stretched exponential to the whole dataset as the gold standard, we computed the error committed by using each of the down sampled datasets in three regions of interest (posterior limb of the internal capsule -IC_P, frontal white matter -FWM, thalamus). Results are reported in the figure S5. In particular the protocol P1 seems to give the most faithful estimation of the gamma metrics, suggesting that the error committed by using less reach protocol is indeed practicable.
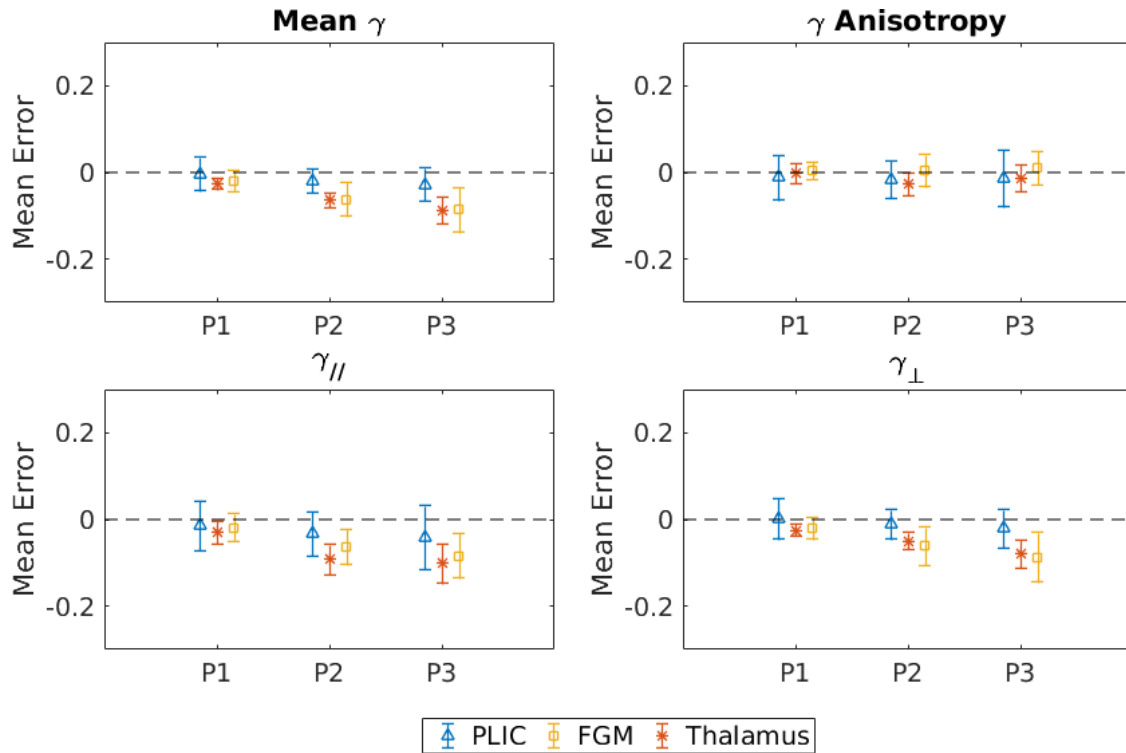
Figure S5: The error committed when fitting the γ model to a down sampled set of diffusion data. The four boxes refer to the different γ-metrics. The error is evaluated only for the protocols belonging to the first set of protocols (i.e. P1, P2, P3) in three regions of interest (ROIs), representing different tissue kinds. The mean error is obtained as the average of the difference of the values using the P0 protocol and the down sampled protocols, in each voxel (e.g. the Mγ mean error of P1 in the PLIC is: $< M\gamma^{P0} - M\gamma^{P1}>_{PLIC}$, with $<.>$ is the average of the voxels belonging to the PLIC).

Table S1: Three different Set of parameters were used to obtain synthetic data. They represent different conditions: set 1 is isotropic effective diffusivity and isotropic values of gamma. Set 2 is an anisotropic effective diffusivity, but with isotropic values of gamma. Set 3 is anisotropic values of effective diffusivity and gamma. The effective diffusivities are in 1e-3 (mm^γ)/ms.

	Deff1	Deff2	Deff3	$\gamma 1$	$\gamma 2$	$\gamma 3$
Set 1	1.0	1.0	1.0	0.7	0.7	0.7
Set 2	1.2	1.0	0.8	0.7	0.7	0.7
Set 3	1.2	1.0	0.8	0.8	0.7	0.6

Table S2: The protocols used to study the effect of down sampling the data on the parameter estimation. P0 is the protocol used in our work. P1 P2, P3 have 5 b-values (instead of 11), distributed in different ways. A1 and A2 have 3 b-values. The b-values are in s/mm^2. All the protocols had the same number of directions in each b-shell (15).

	200	400	600	800	1000	1500	2000	2500	3000	4000	5000
P0	✓	✓	✓	✓	✓	✓	✓	✓	✓	✓	✓
P1	-	✓	-	✓	-	✓	-	✓	-	✓	-
P2	-	-	✓	-	✓	-	✓	-	✓	-	✓
P3	-	-	-	✓	-	✓	-	✓	-	✓	✓
A1	-	-	-	✓	-	-	-	-	✓	-	✓
A2	-	-	-	✓	-	-	-	-	✓	✓	-